Accuracy considerations in MR Image-Guided Neurosurgery

by

Patrice Munger

Department of Physics
McGill University, Montréal

A Thesis submitted to the Faculty of Graduate Studies
and Research in partial fulfillment of the requirements
for the degree of Master of Science.

Contents

List of Figures vii

List of Tables viii

Acknowledgments ix

Abstract xi

Résumé xii

Contributions xiii

List of Symbols and Abbreviations xv

1 Introduction **1**

1.1 Conventional Stereotaxy 1

1.2 Image-Guided Neurosurgery 3

1.3 Image-Guidance System used at MNI 5

1.3.1 The Allegro workstation 5

1.3.2 The Viewing Wand 6

1.3.3 The FARO Surgical Arm . . . 8
1.3.4 Pre-surgical preparation of an IGNS procedure . . . 10
1.4 Accuracy . . . 10

2 Overview of Image-Guided Neurosurgery 13

2.1 Spaces Involved . . . 13
2.2 Measurement in scanner space . . . 18
2.2.1 Image acquisition . . . 18
2.2.2 MR Geometrical Distortions . . . 19
2.2.3 Reformatting . . . 21
2.2.4 Rendering . . . 22
2.3 Registration . . . 24
2.3.1 Homologous point matching . . . 24
2.3.2 Surface Matching . . . 25
2.4 Accuracy of CT based IGNS . . . 26

3 Registration 28

3.1 Registration Error . . . 28
3.2 Comparison between two registrations . . . 29
3.3 Expectation of registration error . . . 30
3.4 Homologous point matching simulations . . . 32
3.5 Registration comparison in the clinical situation . . . 37
3.6 Comparison between individual frame-based registrations . . . 45

4 Accuracy of localizing devices 47

4.1 Experimental Setup 48

4.2 Experimental Protocol 49

4.3 Data Analysis 50

4.3.1 Conversion of OPTOTRAK Data 51

4.3.2 Conversion of FARO Arm Data 52

4.3.3 Relative Accuracy Comparison 53

4.4 Results 54

4.5 Conclusion 56

5 MR geometrical distortion 57

5.1 Distortion of Stereotactic Markers 57

5.1.1 Data acquisition 61

5.1.2 Data analysis 61

5.1.3 Results 63

5.1.4 Conclusion 65

5.2 Field Mapping 68

5.2.1 Three-point Dixon technique 71

5.2.2 Results 74

5.2.3 Conclusion 76

6 Conclusion and Future work 79

6.1 Future Work 81

6.1.1 Characterization of absolute registration error 81

6.1.2 Use of a localizer 82

6.1.3 Optimization of MR pulse sequences 83

6.1.4 Real time monitoring of anatomical changes 83

Bibliography **83**

List of Figures

1.1 OBT (Olivier-Bertrand-Tipal) stereotactic frame. 2

1.2 The Viewing Wand system in the operating room. 6

1.3 The Viewing Wand software main screen. 7

1.4 The FARO Surgical Arm. 8

1.5 Diagram of the FARO Surgical Arm with related devices. 9

2.1 Overview of IGNS. 14

2.2 Transformation giving the reformat plane. 22

2.3 Homologous point matching registration technique. 24

2.4 Surface matching registration technique. 26

3.1 Homologous point matching simulation: 4 homologous pairs, $\sigma_n = 2$ mm. 34

3.2 Homologous point matching simulation: 4 homologous pairs, $\sigma_n = 3$ mm. 34

3.3 Homologous point matching simulation: 10 homologous pairs, $\sigma_n = 2$ mm. 35

3.4 Homologous point matching simulation: 10 homologous pairs, $\sigma_n = 3$ mm. 35

3.5 Homologous point matching simulation: 50 homologous pairs, $\sigma_n = 2$ mm. 36

3.6 Homologous point matching simulation: 50 homologous pairs, $\sigma_n = 3$ mm. 36

3.7 Distribution of rotational error θ. 10 homologous pairs, $\sigma_n = 2$ mm. 37

3.8 Distribution of translational error $|\Delta\vec{T}|$ 10 homologous pairs, σ_n = 2 mm. 38

3.9 Registration comparison results. Patient 1. 40

3.10 Registration comparison results. Patient 2. 41

3.11 Registration comparison results. Patient 3. 42

3.12 Registration comparison results. Patient 4. 43

3.13 Homologous point registration comparison results. 46

4.1 Overview of the measurement apparatus. 50

4.2 The probe tip with respect to the LED and the OPTOTRAK coordinate systems. . . . 52

4.3 Histograms of the FARO arm and OPTOTRAK measurement distributions. 54

5.1 Markers of the OBT frame. 59

5.2 Transverse image of the OBT stereotactic frame marker structure. 60

5.3 Sagittal image of the OBT stereotactic frame marker structure. 60

5.4 Coronal image of the OBT stereotactic frame marker structure. 60

5.5 Channels and intersections labels. 63

5.6 Spin-echo sequence with the gradient echo not aligned with the spin-echo. 69

5.7 Phase relation in three-point Dixon technique with spin-echo acquisition. 72

5.8 Typical gradient-echo sequence. 73

5.9 Three-point Dixon spin-echo acquisitions. 75

5.10 Three-point dixon results for spin-echo images. 76

5.11 Field map from spin-echo sequence. 77

5.12 Three-point dixon results for gradient-echo images. 78

List of Tables

3.1 Summary of simulation results. 33

4.1 Localizing device accuracy comparison results. 55

5.1 Computed intersections of frame markers. 64

5.2 Frame corners distortion. 66

Acknowledgments

I would like to thank:

- Bruce Davey for his work on the modification of the Viewing Wand allowing the data acquisition in the experiment on the accuracy of the FARO surgical arm, for his assistance during the data acquisition and for helpful discussions,
- Robert Rohling from the Biorobotics Lab of McGill University for his contribution to the experiment involving the OPTOTRAK and for providing figures in Chapter 4,
- Rick Hoge for the acquisition of three-point Dixon data,
- Louis Collins, Bruce Pike and Atsushi Takahashi for helpful suggestions and for their patience in answering my questions,
- The Neurosurgeons of the Montreal Neurological Institute, A. Oliver, D. Lacerte, J. Bizzi and M. Munz for their collaboration in operating room,
- Samuel Song, for providing his phase unwrapping program necessary for the computation of field maps,
- The people of the Neuro-Imaging Lab who never hesitated to spend time providing me with their help and
- Natural Science and Engineering Research Council of Canada (NSERC) for financial support.

Finally, I would like to thank my supervisor, Dr. Terry M. Peters, for his support and encouragement, and for the time he spent to read the manuscript of this thesis and suggest ways to improve it.

Abstract

This thesis studies various aspects of the accuracy issue in image-guided neurosurgery (IGNS). Factors such as registration, MR geometrical distortions and accuracy of digitizing device, are theoretically described in a general model of IGNS.

The means of registering the patient to its image data is then studied, starting with the definition of registration error. Computer simulations of registration by homologous point matching are described along with a clinical study comparing homologous point matching and surface matching registration methods.

A 3-D MR geometrical distortion experiment performed on a stereotactic frame is presented. These measurements demonstrate the discrepancy that can be observed in the geometry of the frame when imaged with differing read-out gradient directions, and quantitatively evaluate the geometrical distortion associated with the image of the frame of known geometry.

Since geometrical distortion of MR images can adversely affect the accuracy of IGNS, the three-point-Dixon MR pulse sequence is evaluated as a mean of estimating the magnetic field inhomogeneity, and hence potential geometrical errors in images.

Finally, an experimental comparison of mechanical and optical localizing devices is described, resulting in a quantitative estimate of the precision and accuracy of both systems.

Résumé

Cette thèse étudie quelques aspects reliés à la précision de la guidance neurochirurgicale assistée par ordinateur. Ces aspects, le recallage, la distorsion géométrique des images par résonance magnétique et la précision du dispositif de localisation, sont étudiés théoriquement dans le cadre d'un modèle général de la guidance neurochirurgicale.

Le recallage des images et du patient est ensuite étudié, en commençant par la définition de l'erreur de recallage. Des simulations de recallage par corrélation de points homologues sont décrites avec une étude clinique comparant les techniques de recallage par corrélation de points homologues et par corrélation de surfaces.

Une étude des distorsions géométriques des images de résonance magnétique 3-D faite sur un cadre stéréotaxique est également présentée. Ces mesures démontrent les différences pouvant être observées dans la géométrie des marqueurs du cadre lorsque que différentes direction du gradient de codage en fréquence sont utilisées. Une évaluation quantitative des distorsions des marqueurs du cadre stéréotaxique est également présentée.

Étant donnée l'importance que revêt le problème des distorsions géométriques des images en guidance neurochirurgicale, la technique d'acquisition "three-point Dixon" est évaluée en tant que méthode permettant la quantification de ces distorsions.

Finalement, une comparaison expérimentale de deux dispositifs de localisation de points dans l'espace, l'un mécanique et l'autre optique, est exposée.

Contributions

P. Munger and T. M. Peters. Comparison between point-matching and surface-matching registration procedures for MR image-guided neurosurgery. In *Proceedings of the Society of Magnetic Resonance in Medicine*, page 484, 1994.

Robert Rohling, Patrice Munger, John M. Hollerbach, and Terry Peters. Comparison of relative accuracy between a mechanical and an optical position tracker for image-guided neurosurgery. In Anthony M. DiGioia, Takeo Kanade, and Russell Taylor, editors, *Proceedings of the First International Symposium on Medical Robotics and Computer Assisted Surgery*, pages 277–282, Pittsburgh, Penn., September 22-24 1994. Shadyside Hospital.

Bruce Davey, Patrice Munger, Roch Comeau, Laura Pisani, Andre Olivier, and Terry Peters. Applying stereoscopic image visualization to neurosurgical image guidance. In Anthony M. DiGioia, Takeo Kanade, and Russell Taylor, editors, *Proceedings of the First International Symposium on Medical Robotics and Computer Assisted Surgery*, pages 264–271, Pittsburgh, Penn., September 22-24 1994. Shadyside Hospital.

T. M. Peters, B. L. K. Davey, P. Munger, R. M. Comeau, A. Evans, and A. Olivier. Three-dimensional multi-modal image-guidance for neurosurgery. submitted to IEEE Transactions on Medical Imaging, 1994, 1994.

T. M. Peters, C. J. Henri, P. Munger, A. M. Takahashi, A. C. Evans, B. L. K. Davey, and A. Olivier. Integration of stereoscopic DSA and 3-D MRI for image guided neurosurgery. *Computerized Medical Imaging and Graphics*, 18(4):289–299, 1994.

T. M. Peters, C. J. Henri, A. M. Takahashi, P. Munger, B. Davey, R. Comeau, and A. Olivier. Integration of 3-D MRI and stereoscopic DSA for on-line guidance of neurosurgery. In *Proceedings of the Society of Magnetic Resonance in Medicine*, volume 1, page 160, August 14-20 1993.

Bruce L. K. Davey, Roch M. Comeau, Patrice Munger, Laura J. Pisani, Daniel Lacerte, Andre Olivier, and Terence M. Peters. Multimodality interactive stereoscopic image-guided neurosurgery. In Richard A. Robb, editor, *Proceedings of Third Conference on Visualization in Biomedical Computing*, volume 2359, pages 526–536. SPIE, SPIE, Oct. 4-7 1994.

T. M. Peters, B. Davey, R. Comeau, C. J. Henri, P. Munger, P. Charland, A. Evans, and A. Olivier. On-line stereoscopic image-guidance for neurosurgery. In Lowell Klaisner, editor, *IEEE Medical Imaging Conference, San Francisco*, volume 3, pages 1805–1809, Nov. 4-6 1993. Paper 8M01.

List of Symbols and Abbreviations

e	Euler Constant (2.71828 ...)
γ	Gyromagnetic Ratio of Hydrogen Nucleus
$\imath$	Imaginary Number Unit ($\sqrt{-1}$)
ω	Precession frequency
ω_{cs}	Water-Fat Precession Frequency Difference
π	Pi Constant (3.141592 ...)
2-D	Two-Dimensional
3-D	Three-Dimensional
A/D	Analog to Digital Converter
CT	Computerized Tomography
DSA	Digital Subtraction Angiography
EEG	Electro-Encephalography
Hz	Hertz frequency unit (s^{-1})
LED	Light Emitting Diode
IGNS	Image-Guided Neurosurgery
MNI	Montreal Neurological Institute
MRA	Magnetic Resonance Angiography
MRI	Magnetic Resonance Imaging
MS	Mean Square
OBT	Olivier-Bertrand-Tipal Stereotactic Frame.

OR	Operating Room
PC	Personal Computer
PET	Positron Emission Tomography
RF	Radio-Frequency
RMS	Root Mean Square
RSDS	Root Standard Deviation Square
SVD	Singular Value Decomposition
T1	Longitudinal Relaxation Time
T2	Transverse Relaxation Time
TE	Echo Time
TR	Repetition Time

Chapter 1

Introduction

1.1 Conventional Stereotaxy

Stereotaxy is the methodology involved in the three-dimensional localization of structures within the brain, based on diagnostic image information, and the use of surgical instruments to reach these points. Traditionally, stereotaxy has been used to:

- place electrodes within the brain for stimulation or EEG recording and
- approach deep seated brain lesions with a probe, a canula or a high energy ionizing radiation beam.

Conventional stereotaxy makes use of a frame attached to the patient's head. The OBT (Olivier-Bertrand-Tipal) frame, shown in Fig. 1.1, is currently used at the Montreal Neurological Institute both for relating the patient to the image coordinate systems, as well as a support for surgical instruments in the operating room (OR).

Horsley and Clarke, in 1908, described the first stereotactic procedure on small animals [29]. They used a frame, fixed with respect to external anatomical landmarks, to place electrodes at specific points in the animal's brain. Because this technique was based on the false assumption that the position of an internal point was determined solely by the position of external landmarks,

Figure 1.1: OBT (Olivier-Bertrand-Tipal) stereotactic frame.

it was not precise enough to be used on human subjects.

The next major step in stereotaxy occured in 1947, when Spiegel and Wycis used an imaging technique called pneumoencephalography (which consists in x-ray images of the brain with air injected into the ventricular space) [58]. This provided information about spatial localization of soft tissue landmarks (for example the pineal gland) with respect to the stereotactic frame. Since the specific anatomy of each subject was taken into account, this technique could be used in humans and is the precursor of the first human brain atlas. During this period, Leksell and Riechert [37] in Sweden, and Talairach [61] in France, developed their own stereotactic systems, also based on projection images.

The limitations of all these systems were strongly related to the imaging technique used. Conventional radiographic techniques did not allow unambiguous localization of points in three-dimensional space since they provided only a projection of the subject along one dimension, making the positions of structures perpendicular to the imaging plane indeterminate.

The advent of *Computed Tomography (CT)* [30] gave stereotaxy a new life, providing three-dimensional representations of the subject. Then, it became possible, in principle, to determine from the image set, the position in three-dimensional space of any point inside the brain. Later, *Magnetic Resonance Imaging (MRI)* [36, 10] provided another alternative for stereotaxy, offering anatomical information complementing that of CT. Moreover, *Digital Subtraction Angiography (DSA)* [63] and *Magnetic Resonance Angiography (MRA)* made their appearance, making possible the three-dimensional representation of vasculature. *Positron Emission Tomography* (PET) has also proved itself useful to provide functional information.

The basis of any stereotactic procedure is the establishment of a reference coordinate system common to both the diagnostic information provided by the images (image space) and the patient's space (surgical space). This relies on the ability to localize the same objects or structures in both spaces, a function that is provided by the stereotactic frame. Typical stereotactic frames use N-shaped markers (for CT or MRI) or point markers (for DSA) that allow the position of structures within a volume to be determined unambiguously [28, 20]. Galloway *et al.* [18] presents a comparison of the accuracy of four different frame-based stereotactic systems.

Until recently, stereotaxy was confined to the pre-surgical planning of procedures. Image-guided neurosurgery (IGNS), on the other hand refers to the guidance, on the basis of images, interactively during the procedure. Moreover, IGNS allows the guidance in open-cranium surgeries, which is not possible in conventional stereotaxy because of the presence of the frame.

1.2 Image-Guided Neurosurgery

Neurosurgeons are confronted with a number of issues complicating their work in open-cranium interventions [19]:

- the fact that the brain is completely surrounded by bone makes the approach of the surgical target more difficult than for surgeries on other parts of the body,

- often, critical structures or vessels limit the choice of possible trajectories to reach the target and

- tissue to be resected is not always visually distinguishable from healthy tissue.

IGNS[a] arose from the need to address these issues. Its role is to provide a surgeon with the means to visualize the image of a hand-held probe in relation to the diagnostic image information interactively during surgery. Although CT and MR images are generally used, other modalities may also be integrated [47, 48, 27] (e.g., PET, DSA, MRA, EEG, Video). Additionally, stereoscopic images can provide depth perception, which is useful for interpreting both DSA images and general 3-D volume reconstructions [11, 12].

Transformations involved in conventional stereotaxy map between two-dimensional and three-dimensional spaces. It is, however, possible to think about a set of sectional images as defining a volume, so the notion of a slice is then no longer essential. This makes it possible to find a three-dimensional transformation between the patient and image spaces. This “volumetric” approach has the advantage that only one transformation is required to link the two spaces, and there is no need to compute a different transformation for each slice. In the same way, the reference role of the reference stereotactic marker is no longer essential; it can be replaced by any structure (natural or artificial) visible on the patient and in the images. On the other hand, this approach makes assumptions about the relative position of the slices, which may not be rigorously respected in reality. For instance, it is assumed that the distance between slices is constant, and that there is no rotation between two contiguous slices, that the scaling from on slice to another is the same, etc. Lemieux *et al.* [38] have demonstrated that, in general, the three-dimensional transformation leads to a less accurate mapping of the points from one space to the other, when compared to a two-dimensional transformation computed on a slice-by-slice basis. This can be understood by the fact that a set of 2-D transformations can be seen as a piecewise linear transformation; it

[a] The term Image-Guided Neurosurgery is often used interchangeably with *Frameless Stereotaxy*. We think however that the latter term is not entirely suitable since it implies that conventional stereotaxy can be replaced by frameless techniques. In fact, in the actual state of the art, IGNS and Stereotaxy cover different, non-overlapping domains of applications. Moreover, the use of the stereotactic frame is not even near to becoming obsolete.

is then likely to provide a more accurate match in any given slice than a global transformation.

1.3 Image-Guidance System used at MNI

1.3.1 The Allegro workstation

In order to create a 3-D model of the patient's head and brain surfaces from MRI, the data must first be segmented. In our clinical environment this is performed on an *Allegro* workstation, a product of ISG Technologies[b], where the image is segmented by thresholding its intensity to the desired value. Whenever this technique fails to give an accurate contour of the region of interest (due to image artifacts or poor contrast between the skin and the background), the user can manually correct the contour. User interaction of this type is also used for the segmentation of internal brain structures and lesions [62].

The preparation of a typical IGNS procedure involves the following steps. First, a three-dimensional MR or CT volume must be acquired. In some cases, extrinsic fiducial markers are desired to increase the number of visible landmarks, and they must be placed on the patient's head prior to scanning. The next stage involves the transfer of data from the scanner to the Allegro workstation. Then, segmentation of the skin, brain, lesion and other relevant internal structures is performed. This is largely a manual procedure and can take from 20 minutes to two hours, depending on the number and complexity of structures to be segmented and on the number of slices in the data set. The resulting contour data are then processed to form 3-D reconstructions of the surface of the segmented structures. The original acquisition data along with reconstructed three-dimensional objects are then transferred to a second workstation in the operating room.

[b]Mississauga, Ontario, Can.

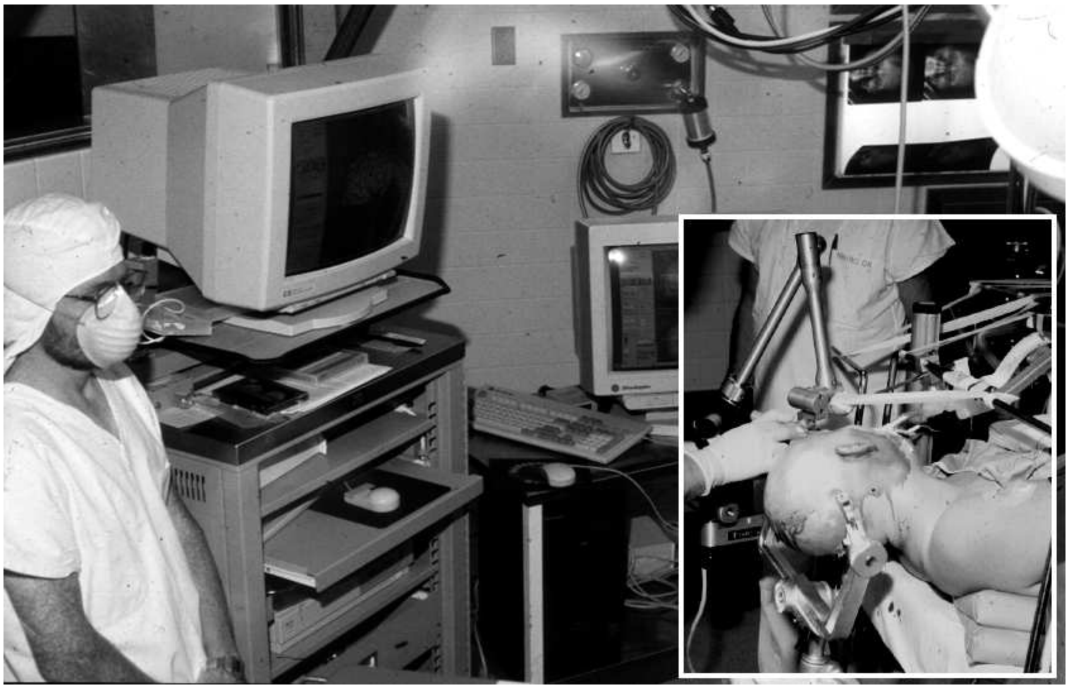

Figure 1.2: The Viewing Wand system in the operating room.

1.3.2 The Viewing Wand

The system used in Operating Room, “The Viewing Wand” (Fig. 1.2), is another ISG product. It imports images and segmented data from the Allegro via magnetic tapes. The software runs on a standard HP Unix workstation (Fig. 1.3) and offers the following features:

- two-dimensional views of the volumetric data in any reformat plane (axial, sagittal, coronal, parallel or perpendicular to the probe),
- three-dimensional surface rendering of any segmented object,
- 3-D objects may be cut or be viewed with transparency,
- registration by homologous point matching and by surface matching of image and patient and
- navigation within the volumetric data by showing the current position of the localizing device. In 2-D, a cross-hair indicates the position of the pointing device while in 3-D, this

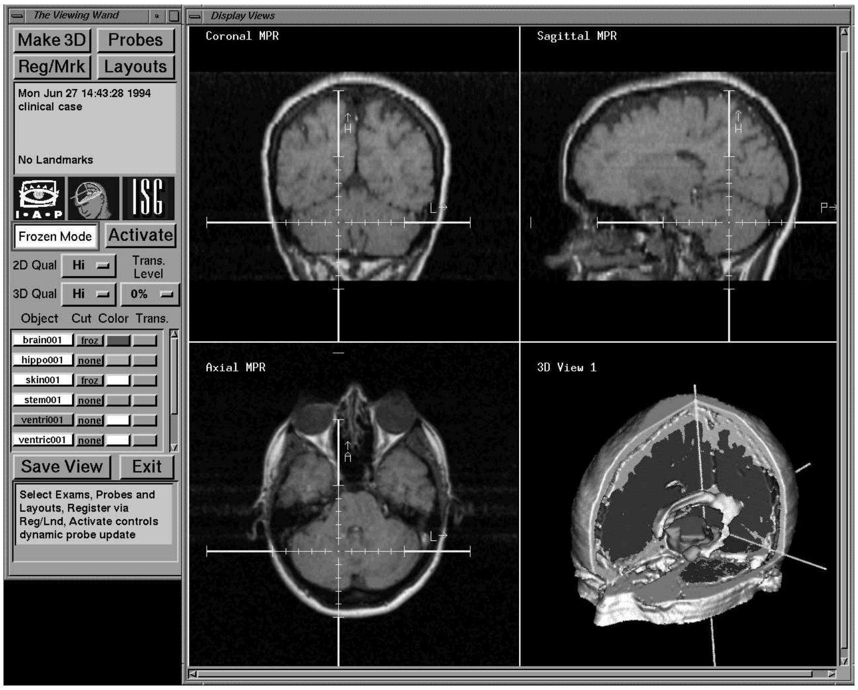

Figure 1.3: The Viewing Wand software main screen.

is achieved by showing a rendered image of the probe in relation with other 3-D objects.

Although segmentation is currently performed on a different machine than the one used in the operating room, it is expected that shortly, all the facilities will be included in a single unit[c]. In addition, a research version of the Viewing Wand developed at the MNI contains the following additional features [13]:

- integration of PET, MRA and DSA imaging modalities and
- stereoscopic display of any 3-D reconstructed surfaces, of maximum intensity projection MRA data, or of DSA projections.

[c]At the time this thesis was written, a set of basic segmentation tools was already included in the Viewing Wand environment.

Figure 1.4: The FARO Surgical Arm.

1.3.3 The FARO Surgical Arm

An integral component of IGNS is a device (mechanical, optical, ultrasonic or magnetic) that allows points in three-dimensional space to be localized and their spatial coordinates transmitted to a computer. The Viewing Wand system installed in the OR at the MNI uses a mechanical localizer, the FARO [d] arm, shown in Fig. 1.4. It is a six degree of freedom articulated arm constructed from aluminum. A probe, consisting of a 200 mm long cylinder with a thin shaft at its end, is attached to a probe holder at the end of the arm. The articulated arm is passive, meaning that the surgeon (or an assistant) manipulates it and holds it in a desired position. The analogue signals produced by the six angle potentiometers located at the joints, are digitized by an analogue-to-digital (A/D) converter interfaced to a PC, which transforms the digitized readings of the joint potentiometers into a set of six numbers representing the position and the orientation of the probe holder with respect to a coordinate system attached to the base of the arm (Fig. 1.5). Further calculations, which depend on the dimensions of the probe used, must then be performed to determine the position of the tip of the probe (see Chapter 4 for more details).

[d] FARO Medical Technologies, Orlando, Florida, USA

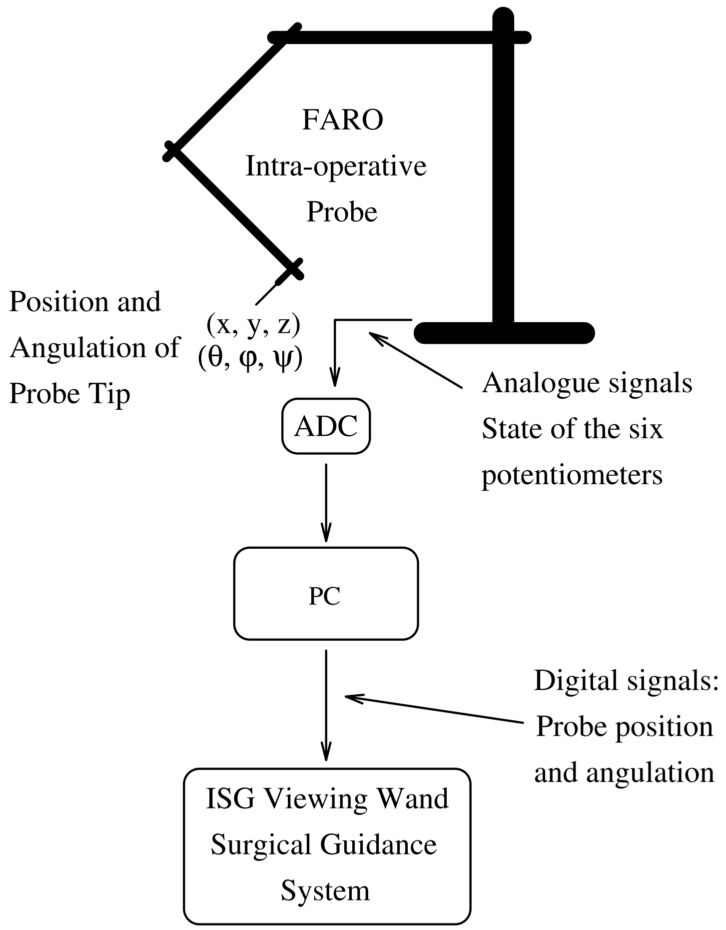

Figure 1.5: Diagram of the FARO Surgical Arm with related devices.

1.3.4 Pre-surgical preparation of an IGNS procedure

Once the acquisition and 3-D reconstruction data have been loaded into the Viewing Wand workstation, further preparation must be performed before the system can actually be used to guide the surgeon. First, when the anesthetized patient is on the operating table, the FARO arm must be firmly fixed to the Mayfield clamp (i.e., the device that holds the head of the patient in place) to ensure that, if the head has to be moved during the surgery, the arm will keep the same position relative to it.

Secondly, to allow the position of the tip of the probe to be computed by the Viewing Wand, the probe must be calibrated. This is performed by inserting it into a hole at the base of the arm and sampling a few points with the probe at different angles, keeping always its tip in the bottom of the hole. Optionally, a "ball-bar" test can be performed, allowing any failure of the mechanical arm to be readily detected.

Finally, the registration, allowing the patient and image spaces to be correlated, must be performed. This is typically accomplished by homologous point matching, which consists of identifying at least three points on both the patient and the image, or by surface matching, which involves sampling a large number of points on the patient's skin with the probe. Registration will be described further in the following chapters.

Once all these steps have been completed, the surgeon can see a representation of the probe on the computer screen, at the proper location on the image of the patient, and the system is ready to provided guidance during the surgical procedure.

1.4 Accuracy

Surgical image-guidance systems consist of several interacting parts, each having its own intrinsic level of accuracy. The objective of this thesis is to quantitatively characterize the error introduced by some of these elements, namely the registration algorithms, the localizing device and the MR geometrical distortions.

The accuracy in IGNS can be conceived as follows. The registration procedure is used to find a 3-D transformation between the patient and the image. Because of the imperfection of the input data (image and digitized points on the patient's head), the transformation found will not perfectly relate the patient to its image. This suggests that the analysis of the accuracy of IGNS can be performed in two steps.

1. Analyze the behavior of registration algorithms under non-ideal input data, i.e., study the effect of perturbations in the input data on the registration error. This is discussed in Chapter 3.

2. Quantify the possible error on the input data. This is the objective of chapters 4 and 5.

Chapter 2 describes the constituents of IGNS and their mutual interaction in a more detailed manner. Presented in this chapter is a model of IGNS in which the role of imaging, patient's surface digitization, anatomical changes and registration is discussed. This chapter clarifies the manner in which the different elements of IGNS interact to produce the overall result.

The topic of registration is treated in Chapter 3, starting with the definition of the registration error and an analysis of its statistical behavior under conditions of noisy data. Clinical comparison measurements between two registration techniques are also reported.

An experiment, whose goal is to compare the accuracy of a mechanical and an optical digitizing devices against an external reference is discussed in Chapter 4.

Finally, the issue of MR images geometrical distortion is addressed in Chapter 5, in which an analysis of 3-D MR data of the stereotactic frame is performed. Additionally, an evaluation of the use of the three-point-Dixon MR acquisition technique as a method of measuring the magnetic field inhomogeneity is made.

The original contributions of this work are:

- the use of a graphical means of describing the difference between two registrations in 3-D space that has the advantage of clearly showing the three-dimensional spatial dependence of the registration error,

- to show that there exists a simple relationship between the RMS rotational and translational errors and the RMS registration error associated with a registration method and
- to show that relevant statistical information on the translational and rotational error associated with a registration technique can be deduced from the comparison of a large number of registrations and
- to compare homologous point matching with surface matching registration technique applied in the context of IGNS.

Chapter 2

Overview of Image-Guided Neurosurgery

IGNS involves the interaction of many elements, and the objective of this chapter is to present them in a unified framework.

Examination of Fig. 2.1, which presents a general diagram of the different elements constituting IGNS, shows that four spaces are involved: *model space*, *physical space*, *scanner space* and *surgical space*.

2.1 Spaces Involved

Referring again to Fig. 2.1, this section describes in some detail the different spaces involved in IGNS. As a first step, the schematic can be separated into four regions, as follows:

- the left half represents objects in real physical world,
- the right half represents measurements of the geometry of physical objects,
- the top half represents the time of image acquisition and
- the bottom half represents the time of surgery.

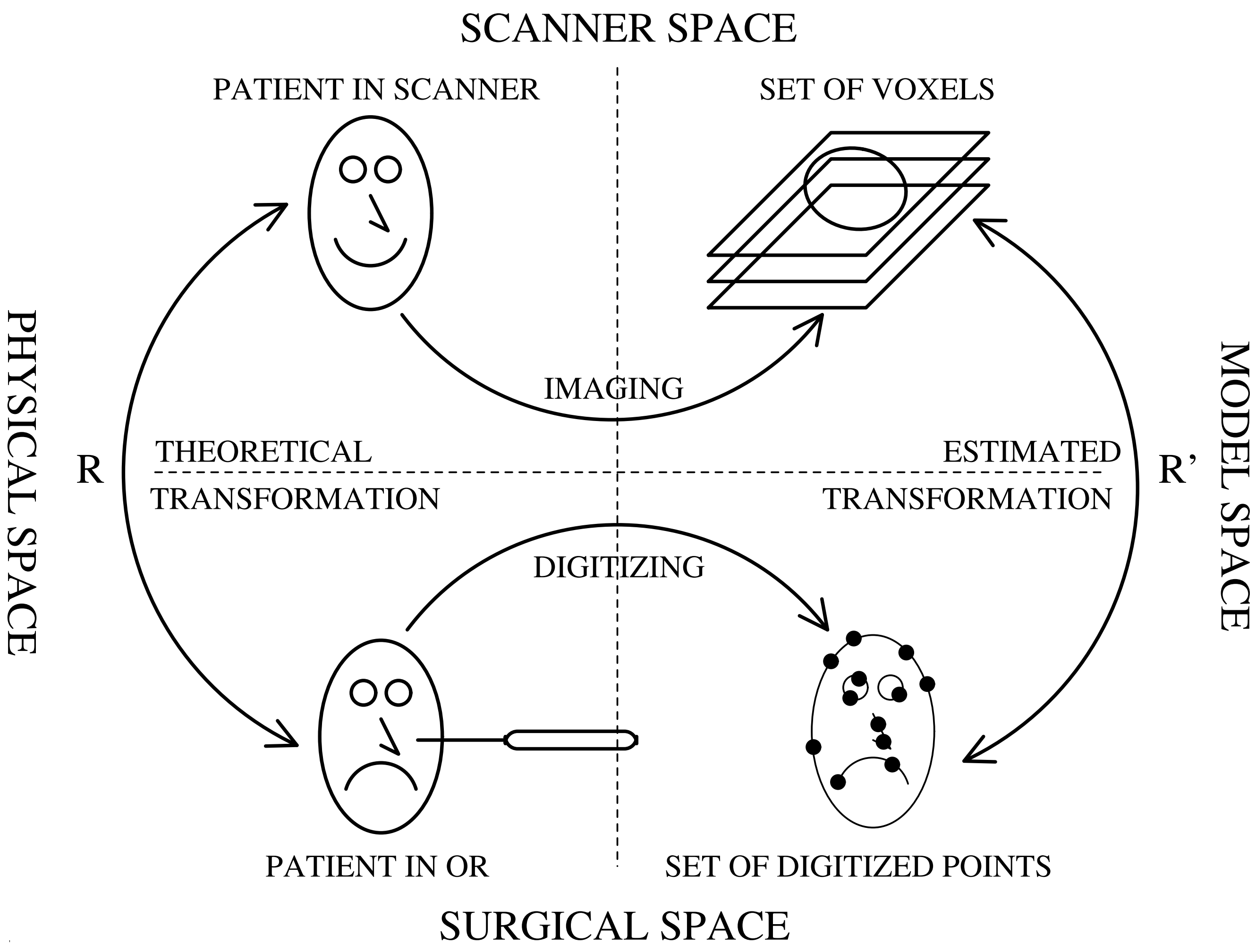

Figure 2.1: Overview of IGNS.

Physical space

Physical space is defined relative to some arbitrary set of 3-D reference coordinates in the real world. The head of the patient in the scanner and in the operating room can be modeled by two volumes in physical space that are related by a non-linear transformation $\mathbf{R}$. This non-linearity arises from the fact that these volumes represent the anatomy of the patient at two different times (the time of image acquisition and the time of surgery), and some anatomical changes might occur between the two situations making the volumes slightly different. However this non-linear part of the transformation between the volumes is expected to be small in any realistic situation. Therefore, we consider the two volumes to be related by a rigid body transformation since in general the rectangular coordinate systems associated with the scanner and surgical spaces are different, i.e., rotated and translated, with respect to each other.

Model Space

Model space can be defined as the digital representation of the two physical volumes that can be processed by a computer. The links between physical and model spaces are provided by some measurement processes. Three factors limit the extent to which the physical volumes are accurately represented in model space.

- Quantization error: Only a finite number of discrete points of the volumes can be measured. Making the computer model continuous implies interpolation between the discrete data points. If the function describing a volume in physical space is not band-limited (which is certainly the case), the interpolation cannot be exact and will introduce errors in the representation of the volume.
- Geometrical distortion error (e.g., field inhomogeneity and flow for MR imaging, slice thickness for CT, pin-cushion for DSA).
- Measurement errors (noise) caused by imperfection of the measuring devices or by the incapacity of the user to precisely localize points in model space. This type of error is expected to be random.

The first goal of any Image-Guided neurosurgical procedure is *to estimate the transformation* $\mathbf{R}$ *between the volumes in physical space by using the imperfect information available in the model space*. The estimated transformation $\mathbf{R}'$ will in general be different from $\mathbf{R}$ because of the errors (mentioned above) introduced in the transformation from physical space to model space. Another error between $\mathbf{R}$ and $\mathbf{R}'$ is introduced by the fact that the non-linear part of $\mathbf{R}$ is not usually taken into consideration in the search for $\mathbf{R}'$. In other words, $\mathbf{R}'$ is chosen to be the rigid body transformation that best matches $\mathbf{R}$. The error caused by this effect increases as the non-linear part of $\mathbf{R}$ (i.e., the deformation between the two volumes) becomes more important. To take the non-linear part of the transformation into account would require the use of non-linear registration techniques [4, 66, 24, 25]. We note here that the main factor contributing to the difference in shape of the patient's head between the scanner space the surgical space are swelling, displacement of tissues due to gravity (since the position of the patient is not necessarily the same in scanner and OR) and expansion or contraction of the brain after craniotomy due to pressure and drug-related effects.

It may not seem obvious why one should be concerned about the deformation of the skin since the region of interest is within the brain. However, registration must be performed before craniotomy and the points to determine the transformation matrix are generally situated on the skin.

Scanner Space

Scanner space defines the coordinate frame in which the images are acquired, with the coordinate system being that of the imaging device. Any point in an acquired image is associated with a physical space position described in terms of the scanner coordinate system. This space is also often referred to as *image space*.

Surgical Space

As its name indicates, this space is associated with the surgical process, where the volume is probed using a digitizing device. At the MNI, a mechanical passive arm is used (see Chapter 1), which allows the three-dimensional coordinates of the location of the tip of the probe to be communicated to the computer. The coordinate system in surgical space is defined by this digitizing device, with the coordinates of a specific point on the patient depending on the relative position between the patient and a reference point associated with this device (for the FARO arm, this reference point is situated at its base). Many varieties of localizing devices have been described in the literature: mechanical [15, 64, 52, 17, 43], ultrasonic [49, 3], optical [26, 5] and magnetic [33].

Mechanical localizers are generally articulated passive arms that can be manipulated by the surgeon. This type of device typically uses potentiometers to determine the angle of flexion of each joint, and from this information, computes the position of the pointer situated at the end of the arm. This type of device can be subject to failure of the mechanical components to which it largely relies and can lose its accuracy after repeated use due to deterioration of these components.

Optical devices use a set of cameras to track the position of light-emitting diodes (LED) by triangulation. This type of digitizer requires that the path between the cameras and the LEDs not be obscured, a condition that can be sometimes difficult to satisfy in the OR. Optical tracking systems are however considered to be more accurate than mechanical arms.

The principle of ultrasonic localizing devices is to determine the position of an ultrasound emitter from the time delay between the emission and the reception of pulses by a set of receivers. The accuracy of type of system, relying on the constance of the speed of sound in air, will be affected by temperature variations. Echo can also constitute a significant accuracy-limiting factor for these systems.

Magnetic localizers use magnetic field gradients, surperimposed on the operating field, that can be detected by a probe. The various magnetic field perturbations coming from ferromagnetic surgical instruments and from radiation from electronic equipment seriously limits the accuracy of such devices in the OR.

2.2 Measurement in scanner space

2.2.1 Image acquisition

We can consider an ideal imaging process as a measurement of a continuous function describing some physical property of the brain. For instance, this property is the x-ray linear attenuation coefficient for CT and x-ray imaging, and the T1 or T2 weighted proton density for standard MR imaging. Even though the images may be actually acquired slice by slice, the ensemble of slices generally constitutes a three-dimensional data set. Each voxel of the acquisition has an intensity value (that is related to the physical property measured) and is associated with a coordinate in scanner space.

The data set can be mathematically modeled as follows. Let $f(\vec{r})$ be the scalar function of space describing the property to be measured. Since any real imaging system has a limit in the spatial frequencies that can be measured, $f(\vec{r})$ must be convolved with the point source response function $g(\vec{r})$ of the imaging system to obtain the measured distribution [65][a]. In CT imaging, the frequency limitation comes from the finite size of the detectors and the size of the focal spot. In MRI, it is a consequence of the limited k-space region that is scanned. The fact that the image is made of voxels is equivalent to multiplying by an array of delta functions. Putting this together, the intensity associated with each voxel, in the ideal case, is

$$\begin{aligned} i(m) &= [\ f(\vec{r}) \star g(\vec{r})\ ]\ \ comb(\vec{r}_m) \\ &= \left[\int_{R^3} f(\vec{s})\ g(\vec{r}-\vec{s})\ \ d\vec{s} \right]\ comb(\vec{r}_m) \end{aligned} \tag{2.1}$$

where m is a label identifying each voxel and $comb(\vec{r}_m)$ represents the function formed by a

[a] This is rigorously true only for linear shift-invariant systems, which is not always the case in medical imaging.

three-dimensional array of δ-functions located at the center $\vec{r}_k$ of each voxel. Equation (2.1) reflects the fact that the measured object property is only known at a finite number of space locations. It must be emphasized that the spacing between the delta-functions in the *comb* must be small enough so that the Nyquist condition is satisfied[b].

2.2.2 MR Geometrical Distortions

Geometrical distortion of MR images is rather significant in the context of IGNS. This section describes this phenomenon, along with some correction methods.

In MR imaging, linear field gradients allow each point in space to be related to a resonance frequency. In one dimension, say x, this can be expressed by:

$$\omega(x) = \gamma\left(B_0 + xG_x\right), \tag{2.2}$$

where B_0 is the main magnetic field intensity, γ the gyromagnetic ratio of the imaged spin and G_x the magnetic field gradient in the x direction. Since any conventional image reconstruction algorithm relies on this relationship, non-uniformity of B_0, non-linearity of G_x or susceptibility effects will introduce errors on the spatial localization of the different resonance frequencies.

It is possible to classify MR geometric distortion source in three main groups [41]:

- machine-dependent,
- patient-dependent and
- stereotactic localizer dependent.

Machine-dependent distortions factors, including main field inhomogeneity, gradient field non-linearity and eddy currents caused by the gradient switching, can in some cases be corrected for by careful calibration of the scanner and by phantom studies. It has been shown [6] that the contribution of gradient non-linearity to the distortion is stable and that it can be corrected for

[b]This still holds for MRI but in this case, the sampling is performed in the Fourier domain, and failure to observe Nyquist condition results in foldover in image space.

independently of the other distortion factors. Also, Michiels *et al.* [41] demonstrate that for 3-D spin-echo and gradient-echo sequences, the spatial misregistration introduced by main field inhomogeneity and gradient field non-linearity is:

$$\Delta x = \frac{\Delta B_0 + \Delta G_x x}{G_x}, \tag{2.3}$$

$$\Delta y = \frac{\Delta G_y y}{G_y}, \tag{2.4}$$

$$\Delta z = \frac{\Delta G_z z}{G_z}, \tag{2.5}$$

where ΔB_0 represents the main field inhomogeneity, ΔG the gradient field non-linearity and x is the direction of the read-out gradient. With the spin warp imaging method, each phase encoding step is performed with a different gradient magnitude (but the gradient is applied for the same time interval). So, the effect of field inhomogeneity in the phase encoding direction is to introduce a space-variant but time-invariant phase shift in that direction (since this gradient is turned off during readout). Since only the magnitude of the complex image is eventually displayed, this phase shift is of no consequence for the final image. Sumanaweera *et al.* [60] describe a method relying on this phenomenon to quantify field inhomogeneity. The principle of this technique is to acquire two images with the readout gradient in orthogonal directions. Any imaged object can be considered to be accurately positioned in the phase encoding direction. In this manner, the true position of the object can be found by combining the information given by the two images. Schad *et al.* [51] describes a geometric distortion study using phantoms of known geometry. One phantom was used to correct for in-plane distortion while another was used to correct for the slice profile distortion. This distortion correction reduced the error on the localization of a target using a stereotactic equipment from 3 mm to 1 mm, where the reference was the localization of the points using a CT scan. However, this method does not allow for correction of distortions induced by patient susceptibility variations. A comparison of the localization accuracy between CT and MR based stereotaxy, made by Kondziolka at al. [34], reports a localization difference around 2 mm between the two modalities. The authors note that the observed difference can be entirely attributed to observer variability in the selection of the target.

Patient-dependent factors, including susceptibility effects, chemical shift and flow, cannot be corrected “once and for all” since they depend on the particular anatomy of each patient. Distortion correction for objects of known shape and composition (fiducial markers for example) can be performed by means of an analysis of the susceptibility distortion induced by such objects. Sumanaweera [59] gives an example of this for a cylindrical fiducial marker. This technique requires the solution of the Laplace equation for the magnetic potential with boundary conditions, which implies that analytical solutions can only be obtained for highly symmetrical objects, and numerical methods must be employed for other cases. The application of this technique for highly variable shapes such as the human head, reported by Shizhe *et al.* [53], gives a good indication of the importance of local magnetic field distortion that can be induced by the patient.

2.2.3 Reformatting

The determination of the image space position corresponding to given physical space location is what IGNS is all about. This can be achieved, once the transformation $\mathbf{R}$ has been estimated (in other words, once $\mathbf{R}'$ has been found), by using the inverse transformation $(\mathbf{R}')^{-1}$. But, in general, an arbitrary point in physical space will map into a point for which the intensity in image space have not been measured (recall that measurement in image space is discrete). Moreover, the surgeon may want to look at the image data through slices in arbitrary orientations (which is in general different from the planes originally acquired). Then, the interpolation of the image data is required, which is performed by reformatting.

Reformatting can be defined in this particular case as *the mapping of image intensities of the model space ($I_{\mathcal{M}}(i, j, k)$) onto the points of an arbitrary plane taken through the model space* [40].

The orientation of the reformatted plane is fully determined if the spatial coordinate of three of its points are known. If $\vec{r}_1$, $\vec{r}_2$, $\vec{r}_3$ are the 3-D position vectors of these points in scanner space and $\vec{s}_1$, $\vec{s}_2$, $\vec{s}_3$, their 2-D positions in the reformatted plane, vectors in scanner space and in the

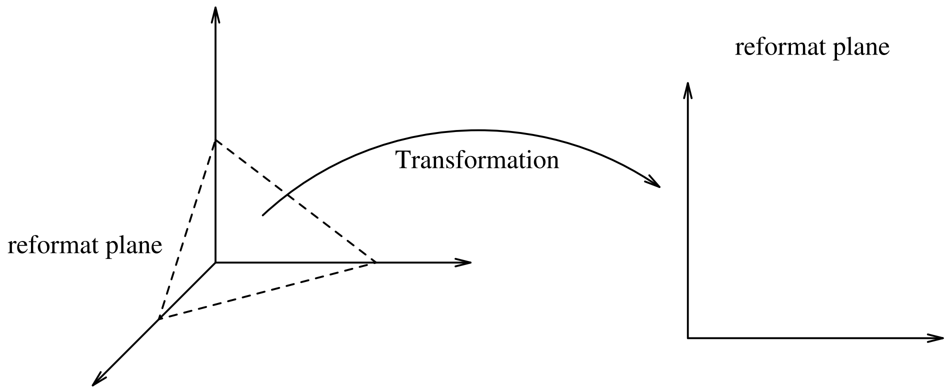

Figure 2.2: Transformation giving the reformat plane.

reformatted plane are related by the following relations:

$$\vec{r} = \mathbf{F} \begin{pmatrix} \vec{s} \\ 1 \end{pmatrix}, \tag{2.6}$$

$$\begin{pmatrix} \vec{s} \\ 1 \end{pmatrix} = \mathbf{F}^{-1} \vec{r}, \tag{2.7}$$

where

$$\mathbf{F} = \begin{pmatrix} \vec{r}_1 & \vec{r}_2 & \vec{r}_3 \end{pmatrix} \begin{pmatrix} \vec{s}_1 & \vec{s}_2 & \vec{s}_3 \\ 1 & 1 & 1 \end{pmatrix}^{-1}. \tag{2.8}$$

Note that $\vec{r}$ and $\vec{s}$ are 3×1 and 2×1 column vectors respectively. Once the transformation $\vec{F}$ has been defined, the values of intensity in the reformat plane can be retrieved from the values in the scanner space.

$$I_{\mathcal{R}}(\vec{s}) = I_{\mathcal{M}}(\vec{r}) \tag{2.9}$$

where $\vec{r}$ is given by Equation (2.6). The fact that the intensity is not known at every arbitrary point implies that the value at $\vec{r}$ must be interpolated from the known values in scanner space.

2.2.4 Rendering

IGNS involves the interaction of the user with data in scanner space. The role of rendering is to provide the user with the possibility of efficiently and accurately localizing points on the imaged volume. The data can be accessed by the user through interaction with either 2-D slices (in arbitrary orientation) or a 3-D representation of the volume.

2-D In order to visualize reformatted images, a further transformation is desirable since the resolution of the video display is generally higher than that of the reformatted images themselves. This transformation can be modeled as an interpolation between the reformatted image points. The interpolated image is

$$f'(\vec{r}) = i(j) \star w(\vec{r}) \tag{2.10}$$

$$= \{ \ [\ f(\vec{r}) \star g(\vec{r}) \ ] \ \ comb(\vec{r}_j) \ \} \star w(\vec{r}) \tag{2.11}$$

where $w(\vec{r})$ is an interpolation function (i.e., the Fourier Transform of a low-pass filter). If the original imaged object is not band-limited (which again, is the case in general), $f'(\vec{r})$ will not be the same as $f(\vec{r})$.

3-D One can choose, on the other hand, to localize points on a three-dimensional rendering of the volumetric data. Surface rendering requires an explicit description of the surface that can be obtained by segmenting the data set, i.e., by identifying the voxels that belong to a given 3-D object. Here again, one can take advantage of the higher resolution of the video display to make the image smoother than the actual data.

Images acquired by magnetic resonance are subject to intensity inhomogeneity. Causes for this are identified by Simmons *et al.* [56] as non-uniform slice profile, bandwidth filtering of data, mistuning of the RF coils and crosstalk between contiguous slices. The negative effect of intensity inhomogeneity appears when intensity-based segmentation of the skin surface is performed prior to surface rendering and registration based on surface matching. A technique for correcting this problem is presented by Lim *et al.* [39].

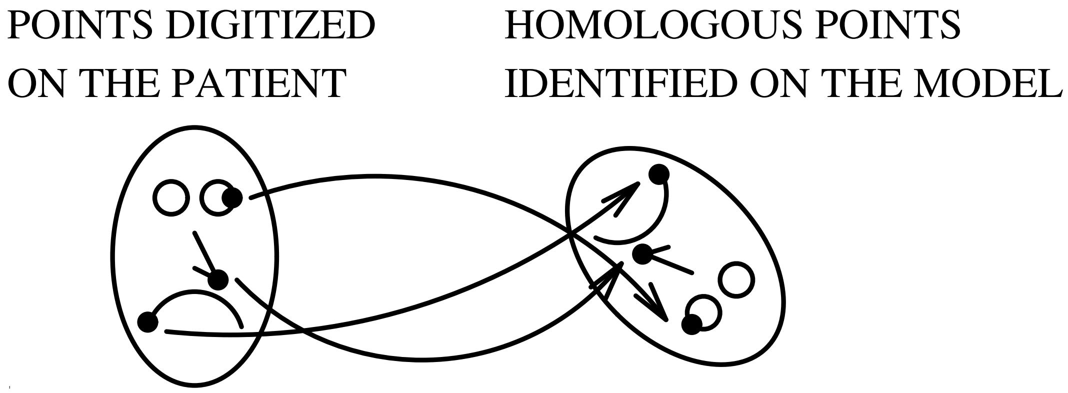

Figure 2.3: Homologous point matching registration technique.

2.3 Registration

Registration is the process that allows the real transformation $\mathbf{R}$ to be estimated using the data available in the model space. Two methods are used in IGNS.

2.3.1 Homologous point matching

This technique uses the fact that a rigid displacement of an object (excluding reflections) can be fully specified by the knowledge of the displacements of three of its points that are non collinear (Fig. 2.3).

Although in a noiseless situation three points is the absolute minimum, more points must be used in practice to ensure that the match is more robust (i.e., less sensitive to uncertainty in the positions of the points). The match is then defined in the least-square sense.

An efficient and stable algorithm for homologous point matching registration uses singular value decomposition (SVD) [2, 54, 55]. This algorithm may be described by considering two $3 \times N$ matrices $\mathbf{A}$ and $\mathbf{B}$ whose columns are the coordinates of points in two spaces related by a rotation. The goal of the registration procedure is to find the rotation matrix $\mathbf{R}$ such that $||\mathbf{A} - \mathbf{RB}||$ is minimum. It can be shown that the least square rotation matrix is

$$\mathbf{R} = \mathbf{VU}^t, \tag{2.12}$$

where $\mathbf{U}$ and $\mathbf{V}$ are the matrices obtained from the singular value decomposition of $\mathbf{BA}^t$:

$$\mathbf{BA}^t = \mathbf{U}\Lambda\mathbf{V}^t. \tag{2.13}$$

Λ is the diagonal matrix whose elements are the singular values, and $\mathbf{U}$ and $\mathbf{V}$ are $3 \times N$ and 3×3 unitary matrices respectively. However, some precautions must be taken when the points are nearly coplanar, since in these cases, the above algorithm can lead to a reflection transformation instead of a rotation. In such situations, the least square rotation matrix is simply obtained by changing the sign of the column of $\mathbf{V}$ that corresponds to the singular value that is close to zero (if there is no such singular value, which is very unlikely, the algorithm fails).

Neelin *et al.* [42] present an extensive analysis of homologous point registration error, using both real and simulated data. One most important conclusion of this study is that for N homologous pairs the registration error goes down as $1/\sqrt{N}$ for $N \geq 10$ when the measurement noise is Gaussian and of zero mean.

2.3.2 Surface Matching

Commonly referred to as the "head and hat" algorithm, this method does not require the identification of homologous points (Fig. 2.4). Instead, it tries to find the best transformation between the surface defined in scanner space (head) and surgical space (hat) by finding the minimum of an objective function of the transformation parameters [40, 44, 45, 46]. The hat points, whose number is typically much larger than the number of points used in homologous point matching, are gathered randomly and uniformly on the surface of the patient's skin. The head is constituted by the 3-D reconstruction of the patient's surface. A starting point for the iterative process can be obtained by performing a rough homologous point match. The iterative nature of this process has the disadvantage that the search could converge toward a local minimum of the objective function.

ISG uses a variation of this algorithm to perform the surface fit [16]. The principle of their approach is to perform a series of homologous point matching iterations. At each step, every point of the hat (measured on the patient's surface by the probe) is associated with its nearest

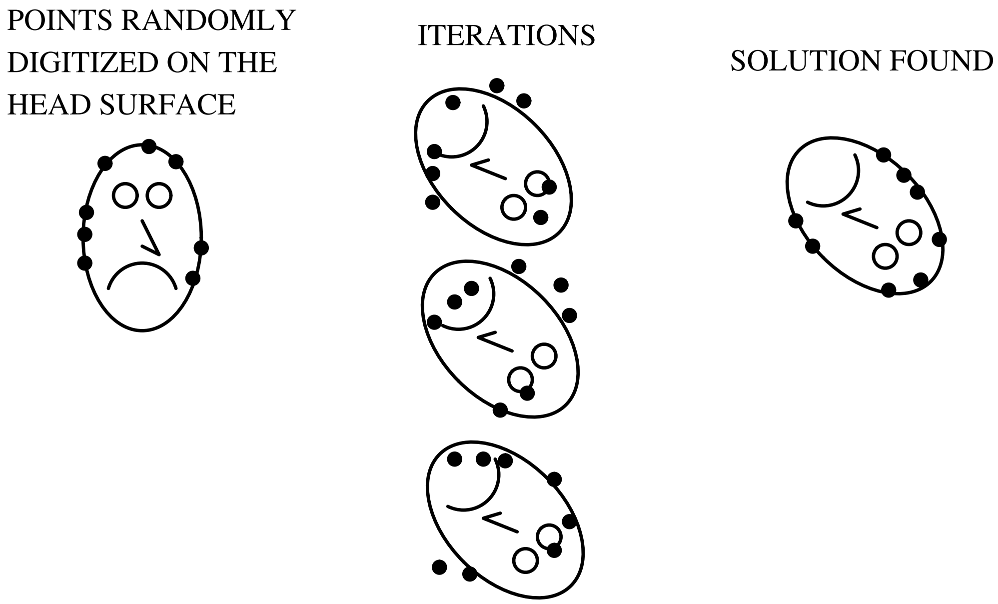

Figure 2.4: Surface matching registration technique.

head point (taken on the reconstructed surface of the patient) to form an homologous pair, and a transformation matrix is computed based on these pairs. The process is stopped when the transformation found at one iteration does not significantly change from that at the previous iteration.

2.4 Accuracy of CT based IGNS

Zinreich *et al.* [67] describe accuracy experiments performed with the ISG Viewing Wand and using CT data. Their experiment consisted of performing homologous point matching registrations with various sets of markers. The main conclusions of this work can be summarized as follows.

- The average error found was 1.7 mm with a standard deviation of 0.9 mm. Maximum errors were between 4 and 5 mm.
- The error was smaller when chosen landmarks were widely dispersed.
- The error was larger when landmarks were in the same plane.

- When landmarks were in the same region, the error tended to increase with the distance from this region.

Chapter 3

Registration

3.1 Registration Error

The registration procedure allows the determination of the linear relationship between two coordinate systems. Let $\vec{x}$ and $\vec{y}$ represent the same vector expressed in two different coordinate systems, and related by the following expression:

$$\vec{x} = s\,\mathbf{R}\,\vec{y} + \vec{T}, \tag{3.1}$$

where $\mathbf{R}$ is a rotation matrix, $\vec{T}$ is a vector giving the translation between the coordinate systems and s is a scale factor. Together, $\mathbf{R}$ and $\vec{T}$ unambiguously describe any arbitrary rigid body transformation. In a real registration, measurement errors will prevent one from finding the exact transformation. In fact the derived transformed coordinate system will in general be slightly rotated, translated and scaled with respect to the exact one. This can be expressed by:

$$\begin{aligned} \vec{x}' &= \Delta s\ \Delta\mathbf{R}\,\vec{x} + \vec{\Delta T} \\ \vec{x}' &= \Delta s\ \Delta\mathbf{R}\,\left(s\,\mathbf{R}\,\vec{y} + \vec{T}\right)\ + \vec{\Delta T}, \end{aligned} \tag{3.2}$$

where $\Delta\mathbf{R} \approx \mathbf{I}$ is a rotation matrix, $\vec{\Delta T} \approx \vec{0}$ is a translation vector and $\Delta s \approx 1$ is the scaling error. Equation (3.2), written as $\vec{x}' = s'\,\mathbf{R}'\,\vec{y} + \vec{T}'$ with $\mathbf{R}' = \Delta\mathbf{R}\mathbf{R}$, $\vec{T}' = \Delta s\,\Delta\mathbf{R}\vec{T} + \vec{\Delta T}$ and $s' = s\Delta s$, clearly demonstrates the fact that one can be mislead by merely comparing the rotation matrices and the translation vectors to evaluate the registration error. Since $\vec{T}'$ depends on $\Delta\mathbf{R}$, a small rotational error can make $\vec{T}$ and $\vec{T}'$ significantly different if the modulus of $\vec{T}$ is large (which is often the case in IGNS).

We define instead the *registration error* $\vec{\Delta}(\vec{x})$ as follows:

$$\vec{\Delta}(\vec{x}) \equiv \vec{x}' - \vec{x}. \tag{3.3}$$

From (3.1) and (3.2):

$$\vec{\Delta}(\vec{x}) = (\Delta s\, \Delta\mathbf{R} - I)\, \vec{x} + \Delta\vec{T}. \tag{3.4}$$

3.2 Comparison between two registrations

It is sometimes desirable to compare registrations between two spaces performed with two different methods or two different conditions of application of one single method. More interestingly, if one registration happens to be "accurate", as verified by independent measurements, the comparison with another method will give a direct measurement of the registration error for that approach.

In the case where two registrations are performed without knowing the "true" transformation, (3.4) can still be used to find the *registration difference* $\vec{\Delta}(\vec{x}_1) \equiv \vec{x}_2 - \vec{x}_1$ between them using:

$$\Delta\mathbf{R} = \mathbf{R}_2\mathbf{R}_1^{-1}, \tag{3.5}$$

$$\Delta s = \frac{s_2}{s_1}, \tag{3.6}$$

and

$$\Delta\vec{T} = \vec{T}_2 - \Delta s\, \Delta\mathbf{R}\, \vec{T}_1 \tag{3.7}$$

where $(\mathbf{R}_1, \vec{T}_1, s_1)$ and $(\mathbf{R}_2, \vec{T}_2, s_2)$ are the registration parameters of the two registrations.

It is more useful in practice to express the registration difference in terms of imaging space coordinates since the centre of the head is usually more or less aligned with the isocenter of the scanner (which is the origin of scanner space). In surgical space, the coordinate system is dependant on the relative position of the pointing device and the head. So, the origin of the surgical space can be away from the patient's head.

3.3 Expectation of registration error

A simple comparison of two registrations is in many cases of little help for determining the characteristics of: 1) the expected registration error and 2) the variability from one registration to the other for a given registration method. This is because in any realistic situation, the true "best" transformation is not known *a priori*. In this section, we analyze the behavior of registration error characteristics averaged over a large number of trials. This provides, at least in principle, a means of characterizing registration methods.

Returning to the formulation introduced in section 3.1, it is interesting to compare not only two registrations but a large number (N) of them. For this, we consider the mean square (*MS*) error as a function of $|\vec{x}|$[a]:

$$\left\langle |\vec{\Delta}(\vec{x})|^2 \right\rangle = \frac{1}{N} \sum_{i=1}^{N} |\vec{\Delta}_i(\vec{x})|^2. \tag{3.8}$$

Using (3.4)[b] and applying the cosine law twice, we observe that:

$$|\vec{\Delta}(\vec{x})|^2 = 2(1 - \cos\theta)|\vec{x}|^2 + |\vec{\Delta T}|^2 - 2|\left(\mathbf{\Delta R} - I\right)\vec{x}||\vec{\Delta T}|\cos\alpha, \tag{3.9}$$

where θ is the angle between $\Delta\mathbf{R}\vec{x}$ and $\vec{x}$, and α is the angle between $(\Delta\mathbf{R} - I)\,\vec{x}$ and $\vec{\Delta T}$. The derivation of (3.9) uses the fact that $|\Delta\mathbf{R}\vec{x}| = |\vec{x}|$ (since $\mathbf{\Delta R}$ is a rotation matrix).

Now, if N registrations are performed, the *MS* error will be:

$$\left\langle |\vec{\Delta}(\vec{x})|^2 \right\rangle = \frac{1}{N} \sum_{i=1}^{N} \left(2(1 - \cos\theta_i)|\vec{x}|^2 + |\vec{\Delta T}_i|^2 - 2|\left(\mathbf{\Delta R}_i - I\right)\vec{x}||\vec{\Delta T}_i|\cos\alpha_i\right). \tag{3.10}$$

If N is sufficiently large the last term in the expression will vanish since α can take any value between 0 and 2π. This will make $\left\langle |\vec{\Delta}(\vec{x})|^2 \right\rangle$ independent of the direction $\vec{x}$. Furthermore, under the assumption that $\Delta\mathbf{R}$ is close to the unit matrix, θ will be small and $\cos\theta \approx 1 - \theta^2/2$. The *MS* registration error then becomes:

$$\begin{aligned} \left\langle \Delta(r)^2 \right\rangle &= \frac{1}{N} \sum_{i=1}^{N} \left(\theta_i^2 r^2 + |\vec{\Delta T}_i|^2\right) \\ &= \left\langle \theta^2 \right\rangle r^2 + \left\langle |\vec{\Delta T}|^2 \right\rangle, \end{aligned} \tag{3.11}$$

[a] Since it is the square of the *RMS* error, it will be refer to as *MS* error.

[b] The mean rotation and translation can be used to determine $\mathbf{\Delta R}$ and $\vec{\Delta}T$.

where r has been used instead of $|\vec{x}|$ and $\Delta(r)$ instead of $|\vec{\Delta}(\vec{x})|$. It is important to note that for any individual registration, the angle θ by itself is of little significance since it depends on the direction of $\vec{x}$. Equation (3.11) shows that the *MS* registration error increases with the modulus of $|\vec{x}|$ and is related to the individual *MS* of θ and $|\Delta\vec{T}|$.

It is also instructive to look at the variability of θ and $|\vec{T}|$ between registrations. This can be performed by computing the variance of $\Delta(r)^2$ defined by[c]:

$$Var(\Delta(r)^2) = \frac{1}{N}\sum_{i=1}^{N}\left(\Delta_i(r)^2 - \left\langle\Delta(r)^2\right\rangle\right)^2. \tag{3.12}$$

Evaluating the squared term in the summation (3.12) shows that:

$$Var(\Delta(r)^2) = \left\langle\Delta(r)^4\right\rangle - \left\langle\Delta(r)^2\right\rangle^2. \tag{3.13}$$

The first term is:

$$\left\langle\Delta(r)^4\right\rangle = \left\langle\theta^4\right\rangle r^4 + \left\langle|\Delta\vec{T}|^4\right\rangle + 4\left\langle\theta^2\right\rangle\left\langle|\Delta\vec{T}|^2\right\rangle r^2. \tag{3.14}$$

Using (3.13) and (3.11), we find:

$$\begin{aligned} Var(\Delta(r)^2) &= \left(\left\langle\theta^4\right\rangle - \left\langle\theta^2\right\rangle^2\right) r^4 + \left(\left\langle|\Delta\vec{T}|^4\right\rangle - \left\langle|\Delta\vec{T}|^2\right\rangle^2\right) \\ &\quad + 2\left\langle\theta^2\right\rangle\left\langle|\Delta\vec{T}|^2\right\rangle r^2 \\ &= Var(\theta^2) r^4 + Var(|\Delta\vec{T}|^2) + 2\left\langle\theta^2\right\rangle\left\langle|\Delta\vec{T}|^2\right\rangle r^2. \end{aligned} \tag{3.15}$$

This equation allows us to estimate the variability of the registration from the standard deviation of the registration error along a radial line. It shows, as in the case of the mean squared error, that the variance of the squared registration error increases with the distance from the origin.

[c]It is unusual to use the variance of the square of a variable (that we will call *VS*) instead of the variance of the variable itself as a measure of its variability. However, there is a simple analytical expression relating the VS of the registration error with the VS of the rotational and translational errors. Such a relationship does not exist between the variance of the first power of these variables. By analogy with the *RMS* value, we will refer to the *RSDS* value (Root of the Standard Deviation of the Squared variable) which has the same units the variable for which it is computed. Although the statistical significance of this quantity is not clear, we believe that it constitutes a valid measure of variability that can be compared for different registration experiments.

3.4 Homologous point matching simulations

This section illustrates the use of Equation (3.11) to analyze homologous point matching registration. The simulation was performed using Matlab and proceeded through the following steps[d].

1. Landmark points in imaging space were randomly chosen in a cubic region of 400 mm on a side, centered at the origin.

2. A rotation matrix $\mathbf{R}$ and a translation vector $\vec{T}$ were chosen randomly.

3. Homologous points in surgical space were generated by transforming imaging space points with $\mathbf{R}$ and $\vec{T}$ according to the equation:

$$x_{surgical} = \mathbf{R}^{-1} x_{imaging} - \mathbf{R}^{-1} \vec{T}. \tag{3.16}$$

   Note that the scale was kept unchanged between the two spaces.

4. Normally distributed random noise with standard deviation σ_n was added to the surgical space points.

5. The homologous point matching algorithm was applied to the two sets of points to find the transformation $(\mathbf{R}', \vec{T}')$, and the squared modulus of the registration error for 10 points from 0 to 200 mm along the x-axis was computed. The choice of the x-axis is arbitrary and of no consequence on the final result since the average result is independent of the direction of the vectors in imaging space. The procedure was repeated from step 1.

6. After a number of repetitions, the means and standard deviations of the squared registration errors were computed for several equally spaced points on the x-axis.

7. A parabola was fitted to the mean squared registration error in order to find the parameters $\langle \theta^2 \rangle$ and $\left\langle |\Delta\vec{T}|^2 \right\rangle$. The square root of these numbers is shown in Table 3.1 for different numbers of homologous points and noise levels (STD). In addition, some graphs of the *RMS* registration error as a function of the distance from the origin are presented

[d]To simplify the description of the procedure, we will refer to imaging and surgical spaces.

Number of points	*Noise STD (mm)*			
	1	2	3	4
4	0.41 1.19	0.81 2.40	1.23 3.63	1.64 4.76
6	0.26 0.81	0.51 1.60	0.76 2.42	1.06 2.24
8	0.21 0.67	0.41 1.32	0.60 1.98	0.82 2.65
10	0.17 0.58	0.35 1.16	0.54 1.74	0.72 2.34
15	0.14 0.46	0.28 0.93	0.41 1.39	0.55 1.86
20	0.12 0.40	0.24 0.80	0.35 1.20	0.46 1.60
25	0.10 0.35	0.20 0.71	0.31 1.06	0.41 1.41
50	0.07 0.25	0.14 0.50	0.21 0.75	0.28 0.99

Table 3.1: Summary of simulation results.

RMS values of the rotational error (first number, in degrees) and the translational error (second number, in mm) for different levels of noise and different numbers of homologous points.

in Figs. 3.1 to 3.6. The solid line represents the parabola (3.11) fit to the data and the error bar length is twice the square root of the standard deviation of the squared registration error. The dashed line represents the fit of (3.15).

Examination of Table 3.1 and the graphs clearly shows the reduction of the RMS registration error with the number of homologous pairs observed in Neelin *et al.* [42]. Furthermore, it can also be observed that the variability of registrations is reduced by increasing the number of homologous pairs used.

In order to verify that $\langle \theta^2 \rangle$ and $\left\langle |\vec{\Delta} T|^2 \right\rangle$ are representative measurements of the registration method, plots of the distribution of the rotational and translational errors (for 10 homologous pairs and noise standard deviation of 2 mm), are presented in Figs. 3.7 and 3.8. These graphs show clearly that the mean values of the translational and rotational error have the highest prob-

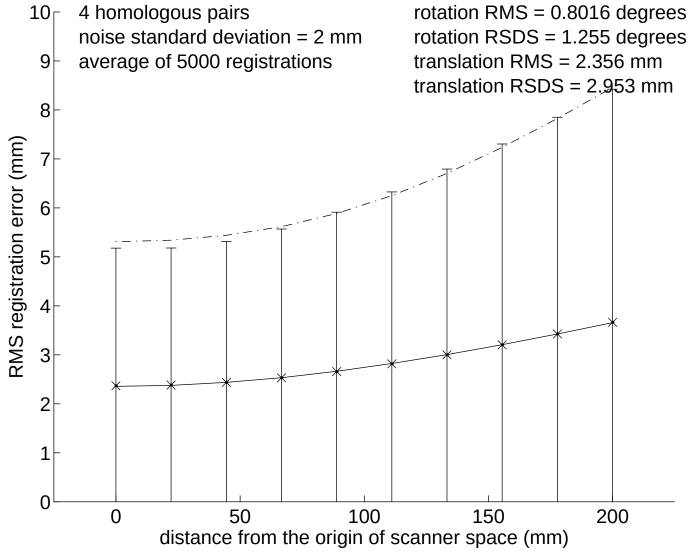

Figure 3.1: Homologous point matching simulation: 4 homologous pairs, $\sigma_n = 2$ mm.

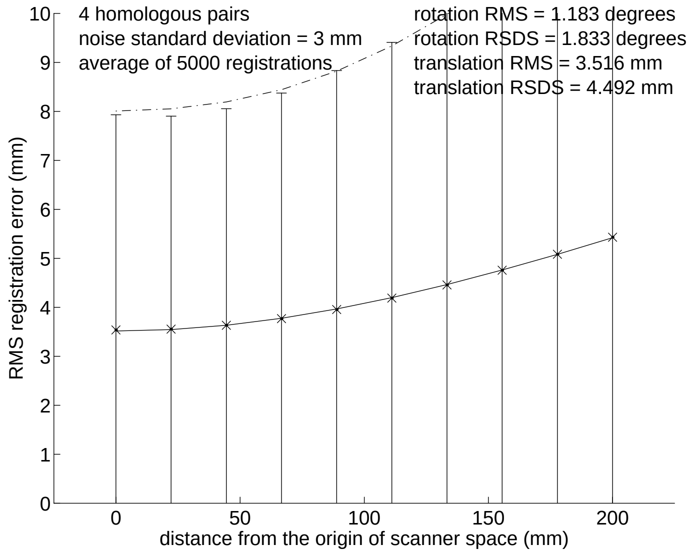

Figure 3.2: Homologous point matching simulation: 4 homologous pairs, $\sigma_n = 3$ mm.

Crosses	RMS registration error
Solid	fit on (3.11)
Dot-Dashed	fit on (3.15)

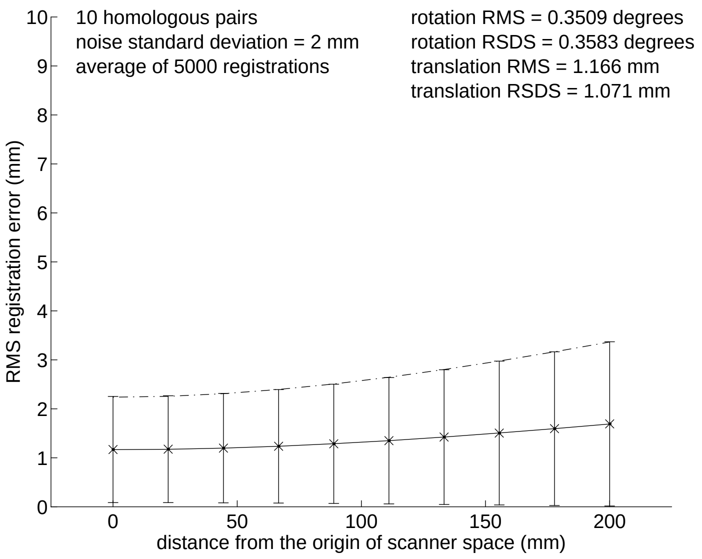

Figure 3.3: Homologous point matching simulation: 10 homologous pairs, σ_n = 2 mm.

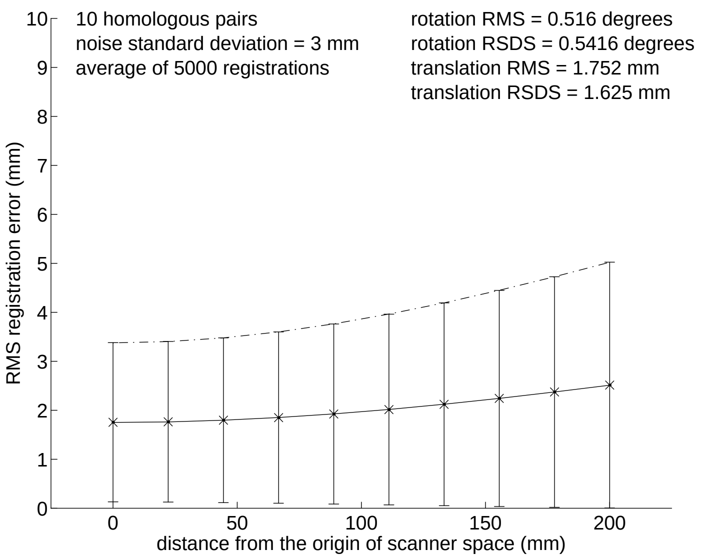

Figure 3.4: Homologous point matching simulation: 10 homologous pairs, σ_n = 3 mm.

Crosses	RMS registration error
Solid	fit on (3.11)
Dot-Dashed	fit on (3.15)

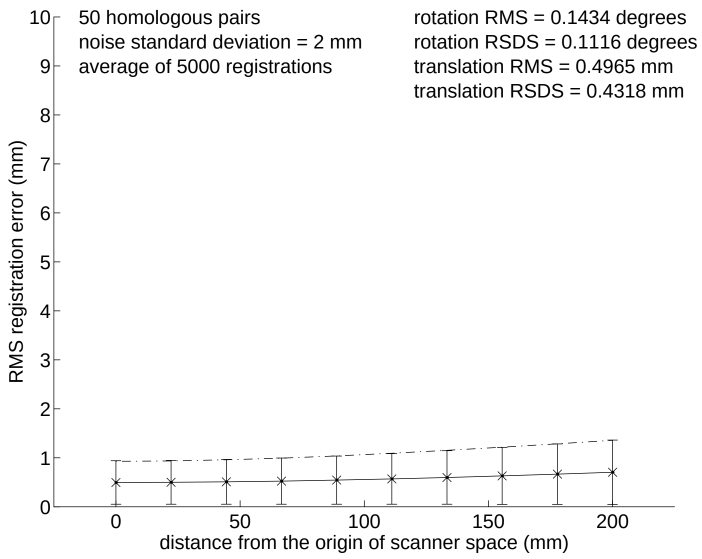

Figure 3.5: Homologous point matching simulation: 50 homologous pairs, σ_n = 2 mm.

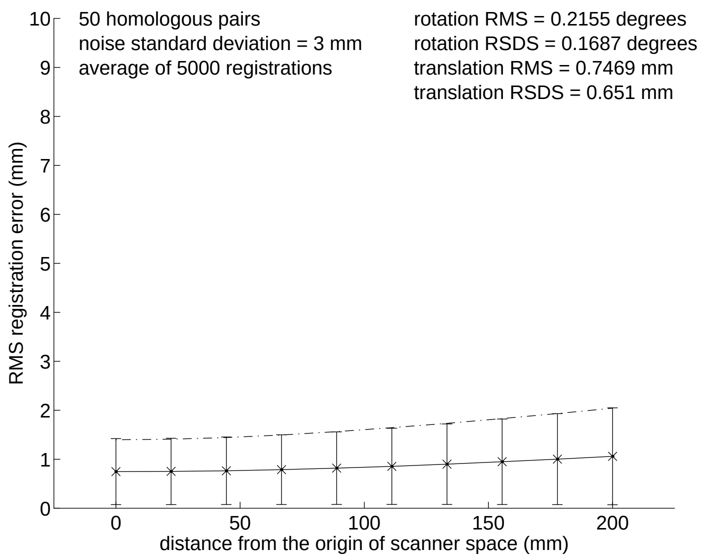

Figure 3.6: Homologous point matching simulation: 50 homologous pairs, σ_n = 3 mm.

Crosses	RMS registration error
Solid	fit on (3.11)
Dot-Dashed	fit on (3.15)

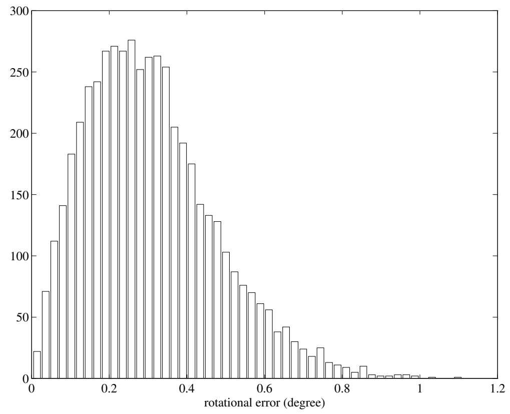

Figure 3.7: Distribution of rotational error θ. 10 homologous pairs, σ_n = 2 mm.

ability of being observed.

3.5 Registration comparison in the clinical situation

The goal of this study was to determine the size of the registration error and the variability involved in registrations performed in the clinical environment (operating room) when IGNS procedures were performed using 3-D images based on MR data. Although these results have a limited statistical significance and bring few insights to the mechanism of registration, they demonstrate that the registration process using MR images is far from trivial, and that the accuracy currently available using the standard approach is $\pm$ 4 mm at best.

These measurements were performed using the following protocol.

1. During a depth electrode implantation procedure, in which the OBT stereotactic frame (see Chapter 1) is installed on the patient's head, two registrations were performed.

    - The first was performed by homologous point matching on the corners of the frame markers (4 points). This was accomplished by touching the intersection of the frame markers using the surgical probe and by selecting the corresponding point in the 3-D data set. Three orthogonal planes were used (sagittal, coronal and axial) to ensure

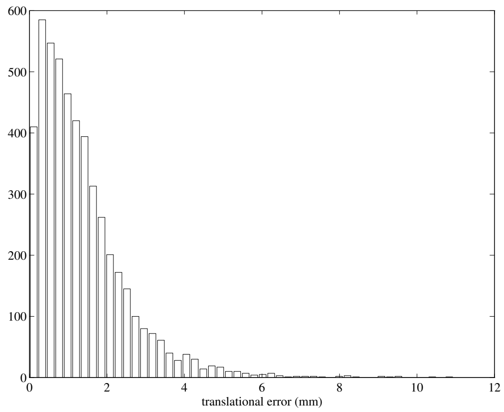

Figure 3.8: Distribution of translational error $|\Delta \vec{T}|$ 10 homologous pairs, σ_n = 2 mm.

an accurate localization of the corner. It must be mentioned that the markers of the frame, being surrounded by a thin layer of Plexiglas, were not directly accessible physically. However, the thickness of the Plexiglas layer was approximately corrected for by selecting points slightly beside the corner seen on the images. The error in the localization of the point in the associated image, however, is probably less than 1 mm.

- The second registration was achieved by surface matching the computer model to the patient's head. The surface points (40) were randomly scattered on the surface. Prior to the surface matching, a rough homologous point match was performed in order to arrive at an approximate solution. This preliminary registration used four anatomical external landmarks, usually the two outer canti and one point on each ear, identified on the 3-D rendering of the skin surface.

2. The registration parameters were extracted from the registration log files that are compiled by the Viewing Wand program. These files contain the rotation matrix $\mathbf{R}$, the translation vector $\vec{T}$ and the scale factor S that constitute the transformation between the imaging and surgical spaces:

$$\vec{x}_{imaging} = s\,\mathbf{R}\,\vec{x}_{surgical} + \vec{T}. \tag{3.17}$$

3. The difference between the two registrations was computed according to (3.4) for points along the three axes of model space. The modulus of the difference was then plotted, as shown in Figs. 3.9 to 3.12.

It is not immediately obvious why these graphs are curved lines, since they represent the distance between two straight lines in 3-D space. However, if the lines are represented as:

$$\vec{r}_1 = \vec{r}_{01} + \alpha t \vec{u}_1 \tag{3.18}$$

$$\vec{r}_2 = \vec{r}_{02} + t \vec{u}_2, \tag{3.19}$$

where α is a scale parameter, $\vec{r}_{01}$ and $\vec{r}_{02}$ are points belonging to the lines, $\vec{u}_1$ and $\vec{u}_2$ are unit vectors parallel to them and t is a parameter labelling points on them, we can compute the difference $D(t)$ between corresponding position t on theses lines:

$$D(t) \equiv |\vec{r}_1 - \vec{r}_2| = \sqrt{\alpha^2 |\vec{u}_1 - \vec{u}_2|^2 t^2 + 2\alpha(\vec{r}_{01} - \vec{r}_{02}) \cdot (\vec{u}_1 - \vec{u}_2)t + |\vec{r}_{01} - \vec{r}_{02}|^2}. \tag{3.20}$$

This will give a "v-shaped" function if:

$$|(\vec{r}_{01} - \vec{r}_{02}) \cdot (\vec{u}_1 - \vec{u}_2)| = |(\vec{r}_{01} - \vec{r}_{02})||(\vec{u}_1 - \vec{u}_2)|. \tag{3.21}$$

So, the graphs are straight if $(\vec{r}_{01} - \vec{r}_{02})$ is parallel to $(\vec{u}_1 - \vec{u}_2)$ or if one of these vectors is zero. In all other cases, the line will be curved.

It can be shown that the curve reaches a minimum value when:

$$t_{min} = \frac{\Delta r_0 \cos\theta}{\alpha \Delta u}, \tag{3.22}$$

where $\Delta r_0 \equiv |\vec{r}_{01} - \vec{r}_{02}|$, $\Delta u \equiv |\vec{u}_1 - \vec{u}_2|$ and θ is the angle between $\vec{r}_{01} - \vec{r}_{02}$ and $\vec{u}_1 - \vec{u}_2$.

In order that the minimum be at the origin, let $t' \equiv t + t_{min}$. Equation (3.20) then becomes:

$$D = \sqrt{(\alpha \Delta u t')^2 + \Delta r_0^2 \sin^2\theta} \tag{3.23}$$

$$= \Delta r_0 \sin\theta \sqrt{1 + \left(\frac{\alpha \Delta u}{\Delta r_0 \sin\theta} t'\right)^2}. \tag{3.24}$$

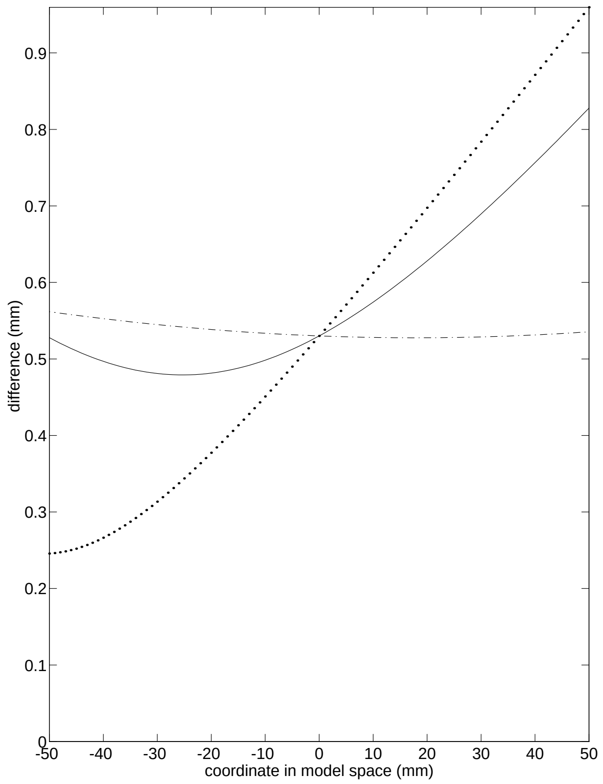

Solid	x-axis
Dotted	y-axis
Dot-Dashed	z-axis

Figure 3.9: Registration comparison results. Patient 1.

Modulus of the registration difference between a homologous point matching and a surface fitting along the three axes of imaging space. This graph shows very little difference between the two registrations. Note that the lines cross at the origin since this point is common to all axes.

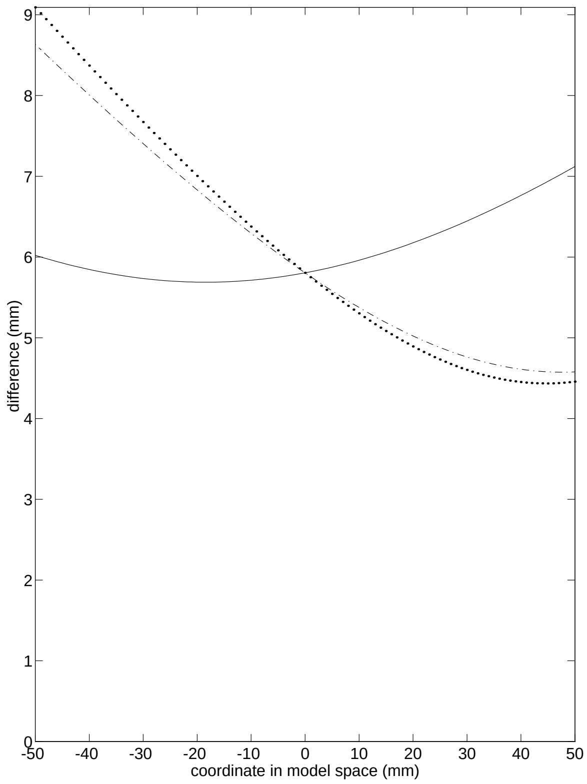

Solid	x-axis
Dotted	y-axis
Dot-Dashed	z-axis

Figure 3.10: Registration comparison results. Patient 2.

Modulus of the registration difference between a homologous point matching and a surface fitting along the three axes of imaging space. Observe that the minimum differences along the y and z axes are not in the center of imaging space. The difference along the x-axis is roughly constant over the range, indicating a large translational error and a small rotational error.

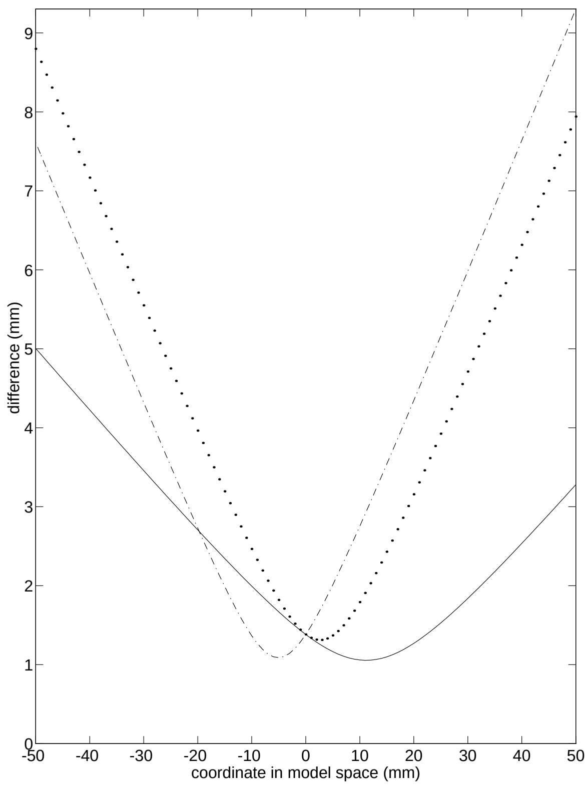

Solid	x-axis
Dotted	y-axis
Dot-Dashed	z-axis

Figure 3.11: Registration comparison results. Patient 3.

Modulus of the registration difference between a homologous point matching and a surface fitting along the three axes of imaging space. The registration difference is small in the center of image space but increases rapidly as one proceeds away from the center. This graph demonstrates that rotational errors can make the accuracy of the registration to vary significantly over the volume of the head.

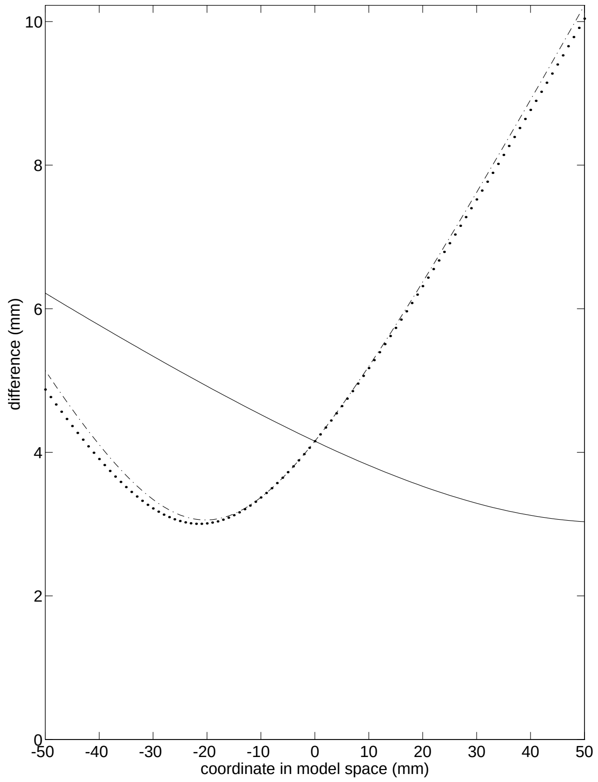

Solid	x-axis
Dotted	y-axis
Dot-Dashed	z-axis

Figure 3.12: Registration comparison results. Patient 4.

Modulus of the registration difference between a homologous point matching and a surface fitting along the three axes of imaging space. The large slopes of the graphs for y and z axes indicate a significant rotational difference around these axes between the two registrations.

When $t' \to \infty$, $D \to \alpha \Delta u t'$ i.e., the distance between the lines increases linearly. When $t' \to 0$, we can develop D in a Taylor series:

$$D \approx \Delta r \sin\theta \left[1 + \frac{1}{2}\left(\frac{\alpha \Delta u}{\Delta r \sin\theta} t'\right)^2\right]. \tag{3.25}$$

This shows that the curvature becomes infinite, i.e., the graph is v-shaped, if $\Delta r_0 = 0$ or $\sin\theta = 0$. If $\Delta u = 0$, i.e., there is no rotational error and $D = \Delta r_0 \sin\theta$ is constant.

Fig. 3.9 shows a sub millimetric difference between the two registrations over the volume of 1000 cubic mm. The situation is quite different for the three other patients, where large differences can be observed. The graph for Patient 2 (Fig. 3.10), reveals a difference at the origin of 6 mm. This means that, if the surgeon holds the probe at the point corresponding the the origin of the scanner space (roughly in the center of the head), the position of the probe displayed on the screen would differ by 6 mm for the two registrations. Moreover, we can see that the minimum difference is around -25 mm along the x-axis and around +40 mm along the two other axes. This illustrates the fact that even though the registration error is likely to be minimum at the origin, it is not always the case. Fig. 3.11 shows an example where the rotational error makes the difference between the two registrations increase rapidly, demonstrating that the registration error can be dramatically space-variant. Since the experimental protocol was consistent across the four patients, we believe that the discrepancy observed between the first patient and the other three is due to statistical fluctuation.

As will be demonstrated in Chapter 5, the image of the corners of the frame markers can be subject to displacements from their real position by approximately 2 mm on average. This, coupled with the imprecision due to the fact that it is not possible to physically reach the intersection points of the markers, makes the uncertainty on the point position to be approximately 3 mm. The observation of Fig. 3.2 shows that the observed errors are certainly possible, although a rigorous comparison is not possible since the curve in Fig. 3.2 and the curves in figures Figs. 3.9 to 3.12 do not represent the same thing (the latter result represents differences between two *different registration techniques* while the first is the expected difference between different registrations performed with *the same registration technique*).

3.6 Comparison between individual frame-based registrations

Further experiments have been performed to evaluate the difference between registrations performed by homologous point matching using the corners of the frame markers. In order to remove the possibility of error introduced by displacement of the images of the fiducials markers in MRI, an equivalent set of CT scans was acquired. Four registrations by homologous point matching were performed using the same protocol as for the clinical study decribed above. The difference between all pairs of registrations is shown in Fig. 3.13.

These graphs clearly demonstrate that the difference between the various pairs of homologous point matching registrations is significantly smaller than the difference between registrations performed with the two different methods reported in the last section. This leads us to conclude that large differences between registrations observed in graphs of Figs. 3.9 to 3.12 are probably due to the variability in the surface fitting registrations. However, additionnal experiments are needed to confirm this. Since these results show the difference between registrations, they are not affected by geometrical distortion of images and conclusions can be extended to MR data sets (only the absolute registration error is affected by geometrical distortion of images).

These data suggest that the use of a homologous point matching procedure on a rigid localization structure leads to more stable (i.e., less variable) registrations (however, it does not establish whether it is more accurate than surface matching registrations). This is seen as a necessary step toward more accurate IGNS, and suggests that further attempts at error reduction be based on a rigid set of fiducial markers.

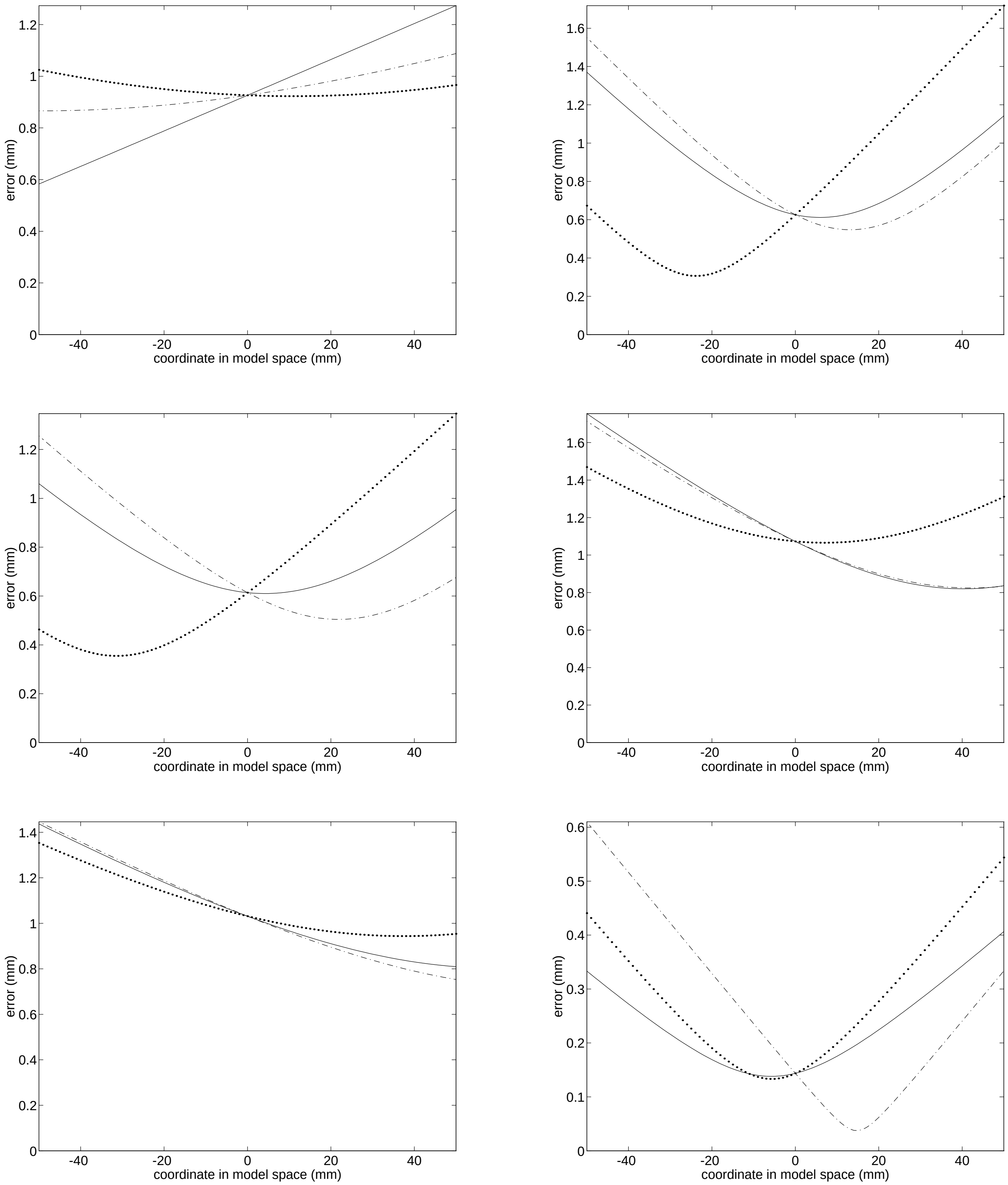

Figure 3.13: Homologous point registration comparison results.

See Fig. 3.9 for the legend.

Chapter 4

Accuracy of localizing devices

The experiment described in this chapter was performed in collaboration with Robert Rohling and Dr. John M. Hollerbach from McGill's Biorobotics Laboratory. The part of the experiment involving the OPTOTRAK would not have been possible without their assistance.

The measurement of the physical volume that constitutes the patient's head is performed using a localizing device that allows the spatial position of a probe to be converted into a set of digital signals representing the spatial coordinates and direction of the probe. Consequently, the accuracy of the localizing device is a factor that directly affects the overall accuracy of an IGNS procedure, and should be measured objectively.

The experiment described here was designed to provide a quantitative estimate of the error introduced by the measurement of the patient's head geometry by the localizing device. Although our main interest was the accuracy of the FARO surgical arm, an integral part of the ISG Viewing Wand system, the experiment was also performed with the OPTOTRAK, an optical localizing device (used by some other groups), since we had access to it through the Biorobotics Laboratory.

The original goal of the experiment was to compare the accuracy of the two localizing devices dynamically, i.e., with the tip of the probe moving along an arbitrary path in space. However it was impossible to synchronize the data acquisition of the OPTOTRAK with the limited sampling rate of the FARO arm, and so a static study of the relative accuracy was performed by comparing the distances between fixed points in space measured by both devices. These measurements were related to a third measurement on a "gold standard", consisting of a metal block, with precisely positioned holes. The motivation for the use of this third independent measurement was to be able to measure the accuracy of the two localizing devices in absolute, rather than relative, terms. This was ensured by the fact that the holes in the reference bar were spaced with an accuracy of more than one order of magnitude better than that of both localizing devices.

The OPTOTRAK is a position tracking device that uses three fixed cameras to track infrared light-emitting-diodes (LED) and determine their position by triangulation. This device has a stated accuracy of 0.15 mm and a resolution of 0.01 mm at a distance of 2.5 m between the LED and the cameras. When multiple LEDs are used, the OPTOTRAK samples them nearly simultaneously ($\sim$1000 Hz bandwidth) at a user selectable sampling rate [31]. On the other hand, the FARO arm has a stated accuracy of 0.5 mm.

4.1 Experimental Setup

The "gold standard" employed in this experiment (which we will refer to as *calibration bar*) was constructed as follows. Holes 15 mm deep and spaced 10 mm apart were drilled into an aluminum bar by a Matsuura MC-510V numerically controlled milling machine[a]. The diameter of each hole was carefully milled to the same diameter than the probe tip such that after the probe was pressed into the hole, no play was detected. The hole was sufficiently deep that the probe tip could descend until an increase of the probe width limited further travel. This milling process, which is accurate to $\pm$ 0.005 mm, ensured that the probe tip would descend the same amount for each hole.

In order to allow the probe attached to the FARO arm to also be localized by the OPTO-

[a]Elliott Machinery (Canada) Ltd.

TRAK, four LEDs mounted onto a small aluminum plate were attached to the probe. This was achieved by inserting the probe in a hole, whose diameter matched the shaft of the probe, reamed into the plate and secured to it by threaded fasteners.

The proprietary program running on the PC that converts the voltages from the FARO arm into numerical signals (see Chapter 1) does not provide the facility to write the probe holder position information directly into a text file. This task was therefore performed by modifying the Viewing Wand software, and required that the entire Viewing Wand system be moved to the location where the experiment took place. The coordinates returned by the FARO arm throughout this experiment were thus furnished by the ISG Viewing Wand to which the arm was interfaced. Note that the role of the Viewing Wand was limited to storing the raw data from the FARO arm, i.e., the capability of the Viewing Wand to compute the position of the tip of the probe was not used.

4.2 Experimental Protocol

The base of the articulated arm, the calibration bar and the OPTOTRAK cameras were all placed in rigid mounts as illustrated in Fig. 4.1. Three calibration trials were undertaken, each with the calibration bar at different positions and orientations with respect to the FARO arm and OPTOTRAK to ensure maximum coverage of the arm's workspace. For each, the following procedure was performed:

- place the probe tip in hole #1,
- remove hands from the probe for a few seconds,
- move probe to next hole and repeat.

During each trial the Viewing Wand program sampled the probe's position at approximately 50 Hz while the LEDs coordinates were sampled by the OPTOTRAK at 100 Hz.

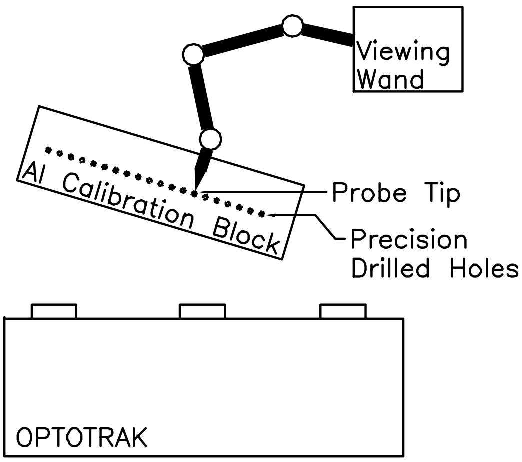

Figure 4.1: Overview of the measurement apparatus.

Fifty FARO arm data samples for the position of each hole were extracted from the stationary portions of the calibration data (i.e., when the operator had his hands removed from the probe), and the same number of OPTOTRAK data samples of each of the four LEDs were extracted in a similar manner.

4.3 Data Analysis

The data collected from each device did not directly give the position of the tip of the probe. Therefore, in order to compare the measurements of the OPTOTRAK and the FARO arm, the position of the actual tip of the probe had to be calculated from these data, in each case. The offset between the tip of the probe and the point to which raw data refer to was determined, for both devices, by a least square fit procedure (described below). This approach has been adopted because it is believed to be more robust than a direct mechanical measurement. Furthermore, the point for which the FARO arm raw data are given (situated in the probe holder) is not accessible physically, making the latter type of measurement impossible.

4.3.1 Conversion of OPTOTRAK Data

As shown in Fig. 4.2, the mean position of the LEDs as determined by the OPTOTRAK gives the vector ${}^{O}\vec{v}_P$. The position of the tip of the probe in the OPTOTRAK reference system is given by the vector ${}^{O}\vec{v}_{tip}$. From the figure, it can be seen that ${}^{O}\vec{v}_{tip}$ can be determined if the vector ${}^{P}\vec{v}_{tip}$ is known together with the orientation of the coordinate system P with respect to O. The vector ${}^{P}\vec{v}_{tip}$ (constant in the P coordinate system) was determined by the following procedure.

The probe was rotated about a fixed endpoint (i.e., ${}^{O}\vec{v}_{tip}$ is constant), 500 measurements were taken and each sample and the centroid of the LEDs (${}^{O}\vec{v}_P$) was calculated. A least squares fit was then performed to find the radius and center of the sphere that best fitted this set of points (since that, during the motion, the centroid of the LEDs moved on a surface of a sphere). The vector ${}^{O}\vec{v}_{tip}$ was then taken to be center of this sphere.

The next step was to establish the LED coordinate system P with an origin at the centroid (${}^{O}\vec{v}_P$) of LEDs. Unit vectors having for direction the principal axis of the LEDs, ${}^{O}\vec{x}_P$, ${}^{O}\vec{y}_P$ and ${}^{O}\vec{z}_P$, were determined by solving the eigenvalue problem outlined in [1], and the axis of the probe coordinate system were taken parallel to these vectors.

Using an homogeneous transformation matrix notation, the transformation between ${}^{O}\vec{v}_{tip}$ and ${}^{P}\vec{v}_{tip}$ can be written:

$$\begin{bmatrix} {}^{0}\vec{v}_{tip} \\ 1 \end{bmatrix} = {}^{O}\mathbf{T}_P \begin{bmatrix} {}^{P}\vec{v}_{tip} \\ 1 \end{bmatrix}, \tag{4.1}$$

where

$${}^{O}\mathbf{T}_P = \begin{bmatrix} {}^{O}\vec{x}_P & {}^{O}\vec{y}_P & {}^{O}\vec{z}_P & {}^{O}\vec{v}_P \\ 0 & 0 & 0 & 1 \end{bmatrix}. \tag{4.2}$$

${}^{P}\vec{v}_{tip}$ was then determined from the inverse of (4.1):

$$\begin{bmatrix} {}^{P}\vec{v}_{tip} \\ 1 \end{bmatrix} = \left({}^{O}\mathbf{T}_P\right)^{-1} \begin{bmatrix} {}^{0}\vec{v}_{tip} \\ 1 \end{bmatrix} \tag{4.3}$$

Once the constant vector ${}^{P}\vec{v}_{tip}$ was determined, the position of the probe tip for any data point was computed using (4.1). Note that the transformation matrix in this equation involves

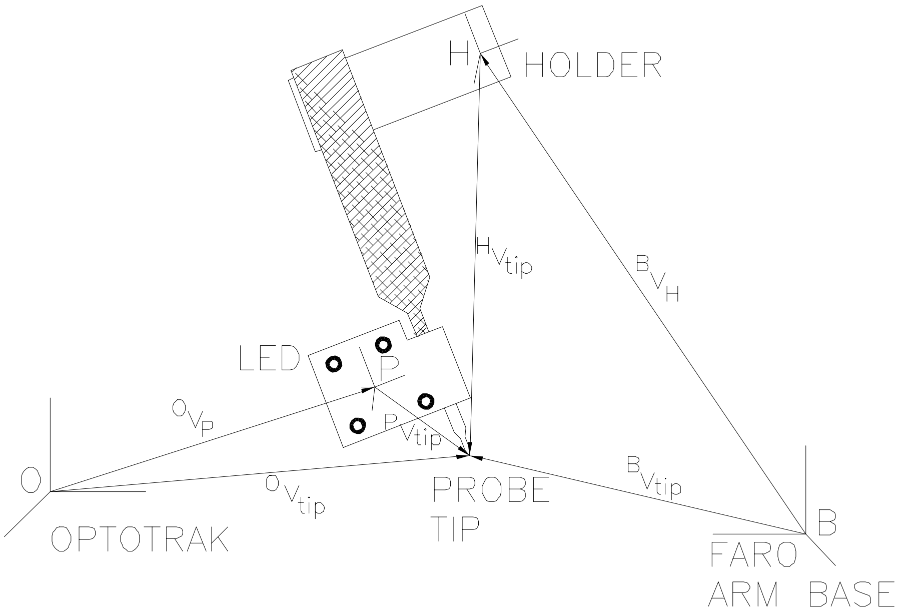

Figure 4.2: The probe tip with respect to the LED and the OPTOTRAK coordinate systems. The following notation is used: O = OPTOTRAK coordinate system, P = Probe coordinate system, H = Probe Holder coordinate system, B = FARO arm base.

the determination of the axis of the P coordinate system.

4.3.2 Conversion of FARO Arm Data

As previously mentioned, the FARO arm data describes the location ${}^{B}\vec{v}_H$ of the probe holder (H) together with its orientation (ϕ,θ,ψ) with respect to a coordinate system attached to the base of the arm (B). The angles correspond to the Euler's angles in the *z*-*x*-*z* convention[b] [23]. The tip position vector ${}^{B}\vec{v}_{tip}$ in the arm's base (B) coordinate system is given by

$$
\begin{aligned}
{}^{B}\vec{v}_{tip} &= [\mathbf{R}_z(\psi)\mathbf{R}_x(\theta)\mathbf{R}_z(\phi)]^{-1}\ {}^{H}\vec{v}_{tip} + {}^{B}\vec{v}_H & (4.4)\\
&= \mathbf{R}^{-1}\ {}^{H}\vec{v}_{tip} + {}^{B}\vec{v}_H, & (4.5)
\end{aligned}
$$

[b]The rotation is specified by three rotations about the z, x and z axis respectively.

where

$$\mathbf{R}_z(\alpha) = \begin{bmatrix} \cos\alpha & \sin\alpha & 0 \\ -\sin\alpha & \cos\alpha & 0 \\ 0 & 0 & 1, \end{bmatrix} \tag{4.6}$$

and

$$\mathbf{R}_x(\alpha) = \begin{bmatrix} 1 & 0 & 0 \\ 0 & \cos\alpha & \sin\alpha \\ 0 & -\sin\alpha & \cos\alpha \end{bmatrix}. \tag{4.7}$$

The homogeneous matrix is written with a notation similar to that in previous section

$${}^{B}\mathbf{T}_H = \begin{bmatrix} & \mathbf{R}^{-1} & & {}^{B}\vec{v}_H \\ 0 & 0 & 0 & 1 \end{bmatrix} \tag{4.8}$$

A separate set of measurements obtained as the probe was rotated about a fixed endpoint was acquired in the same manner as in previous section. Since, during this motion, the tip of the probe was stationary, the vector ${}^{H}\vec{v}_{tip}$ was found by minimizing the standard deviation of the set of tip positions calculated using the inverse of the equation:

$$\begin{bmatrix} {}^{B}\vec{v}_{tip} \\ 1 \end{bmatrix} = {}^{B}\mathbf{T}_H^{-1} \begin{bmatrix} {}^{H}\vec{v}_{tip} \\ 1 \end{bmatrix} \tag{4.9}$$

This value of ${}^{H}\vec{v}_{tip}$ was then used in (4.9) to find the position of the probe's tip (${}^{B}\vec{v}_{tip}$) from the probe holder position and orientation calibration measurements.

4.3.3 Relative Accuracy Comparison

For each of the calculated OPTOTRAK vectors ${}^{O}\vec{v}_{tip}$ and FARO arm vectors ${}^{B}\vec{v}_{tip}$:

- the mean vector to hole #1 location was determined as the mean of 50 samples, obtained for this hole from both measuring devices,
- the 50 samples obtained for hole #2 were subtracted from these from the hole #1 mean vector to obtain the vectors between holes #1 and #2 and

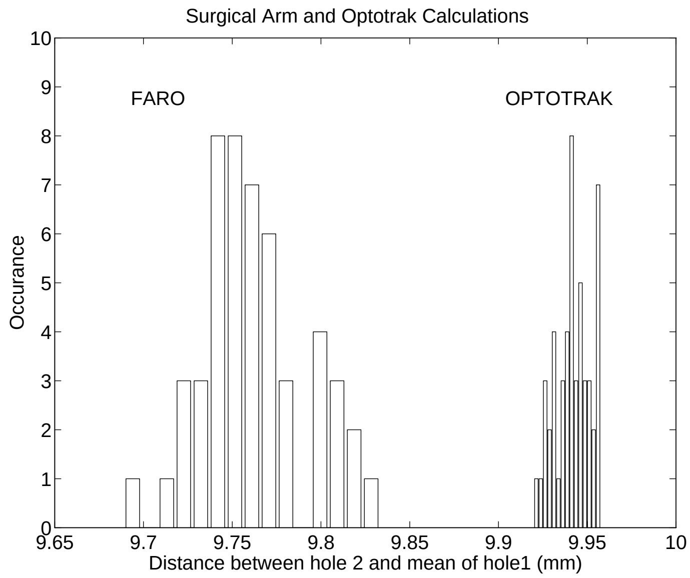

Figure 4.3: Histograms of the FARO arm and OPTOTRAK measurement distributions.

- The norms of each of the 50 difference vectors were determined to find the magnitude of the distance between holes.

This procedure was repeated for all holes measured during each trial.

4.4 Results

The difference in the measured distances between holes #1 and #2 in Trial 1 is plotted in Fig. 4.3. Both the data generated by the OPTOTRAK and the FARO arms yielded distributions close to the true 10 mm spacing. The first point of interest in this figure is that the OPTOTRAK distribution has a mean closer to the true 10 mm spacing than the that of the FARO arm distribution (within the milling machine's 0.005 mm accuracy). Second, the distribution of the OPTOTRAK measurements have a smaller standard deviation than the FARO ARM distribution. The mean of each of the OPTOTRAK and FARO arm distributions are listed in Table 4.1 along with the spread (i.e., the difference between the maximum and the minimum value) of each.

Distance from hole 1 (mm ± 0.005)	OPTOTRAK measured distance [spread] (mm)	FARO arm measured distance [spread] (mm)
Trial 1		
10	9.942 [0.037]†	9.762 [0.144]†
20	-	-
30	-	-
40	39.826 [0.123]	39.434 [0.226]
50	-	-
60	-	-
Trial 2		
10	10.074 [0.152]	10.108 [0.491]
20	20.038 [0.088]	20.057 [0.349]
30	30.082 [0.039]	29.942 [0.162]
40	40.042 [0.048]	39.985 [0.166]
50	50.117 [0.034]	50.008 [0.241]
60	60.115 [0.040]	59.926 [0.195]
Trial 3		
10	9.940 [0.129]	9.718 [0.333]
20	19.868 [0.326]	19.638 [0.369]
30	29.944 [0.187]	29.624 [0.196]
40	39.955 [0.189]	39.456 [0.128]
50	49.823 [0.183]	49.511 [0.545]
60	-	-

Table 4.1: Localizing device accuracy comparison results.

The OPTOTRAK and FARO arm measured distances represent the mean distances between the holes. The spread indicates the difference between the maximum and minimum distances. The data marked with † are plotted in Fig. 4.3.

4.5 Conclusion

The OPTOTRAK gives closer distances to the true 10 mm spacing of the holes in the calibration bar than the FARO arm, the mean error being 0.09 mm. It also delivers smaller spreads for each hole. The measured accuracy of both the OPTOTRAK and FARO arm devices closely matches the manufacturer's specifications. Generally the FARO arm determinations of hole spacing are within 0.5 mm, with a mean value of 0.24 mm, and have spreads of 0.5 mm. However, some distances are determined more accurately, with 0.1 mm not being uncommon.

Although the accuracy of the surgical arm has been accessed for only a small fraction of the entire spatial range of the device, we do not expect large differences in its behavior in other regions.

Even though this experiment shows that the OPTOTRAK is a more accurate localizing device than the FARO surgical arm, we believe that the latter is adequate for surgical applications because its accuracy is significantly better than the current accuracy level observed in IGNS based on MR images. However, in any attempt to increase the accuracy of IGNS the issue of the localizing device accuracy must be addressed more thoroughly.

Chapter 5

MR geometrical distortion

Geometrical accuracy of images is an essential prerequisite for good registrations and for reliability of IGNS. Any geometrical distortion in an MR data set increases the uncertainty on point localization in model space and, as shown in Chapter 3, increases the RMS registration error across the volume of the head.

5.1 Distortion of Stereotactic Markers

One of the most fundamental distinctions between IGNS and conventional stereotaxy is the use of a global 3-D transformation between the image and surgical spaces. In conventional stereotaxy, since the transformation is performed on a slice-by-slice basis, any local distortion in a region of image space does not perturb the transformation found from slices that are removed from that region. However, in IGNS, it is important to ensure that the whole volume is geometrically consistent in order to be able to perform reliable registrations.

Moreover, results of simulations reported in Chapter 3 tend to demonstrate that a means of significantly decreasing the error of registration by homologous point matching is to use a large number of points. Because the number of reliable natural landmarks at the surface of a patient is small, this involves the use of some external set of fiducial markers. These markers could be individually attached to the patient's head or could be fixed to a rigid structure that would itself be firmly attached to the patient's head. In any case, IGNS requires that the markers be accurately represented in image space, i.e., that the relative distribution of the markers as deduced from the images be the same as the actual placements.

In order to test the geometrical accuracy of the representation in image space of such a set of fiducial markers, the relative position of the markers must be known precisely. Since a reference structure specially designed for IGNS is not yet available, the OBT stereotatic frame (Fig. 1.1) was employed instead.

This section describes an experiment whose goal is:

- to measure the geometrical distortion, on a 3-D MR acquisition, of fiducial markers associated with the stereotactic frame and
- to investigate the effect of the image acquisition protocol on the geometry of that structure.

The marker structures visible on MR images of the OBT frame are $CuSO_4$ solution filled channels embedded in plastic plates. Although only four plates were used for the experiment, the frame can accommodate five, and in each of them, four linear channels form a perfect square (of 130 mm on a side) with a fifth channel joining opposite corners of this square. The plates can be fixed on the frame at precise positions. Fig. 5.1 shows the 3-D structure (whose geometry is known to within $\pm$ 0.1 mm) formed by the markers when the plates are mounted on the frame.

In MRI, it is possible to acquire a volume as a whole in one single acquisition (as distinct from 2-D imaging where the volume consists of a stack of 2-D images). This is achieved by manipulating the spin distribution using three orthogonal gradients in such a way that each sample of the MR signal corresponds to a point in a 3-D Fourier space (k-space). Note that unlike 2-D MRI where only one slice is excited at each RF pulse, the signal in 3-D MRI comes from all the spins in the volume. As in 2-D Fourier MRI, one of the gradients is turned on during the readout of the signal. This gradient is referred to as *frequency encoding* or *readout* gradient. The two other gradients are called *phase encoding* gradients. Although in 3-D imaging, since the data are acquired as a volume, the concept of slice is rather imprecise, and it is conventional

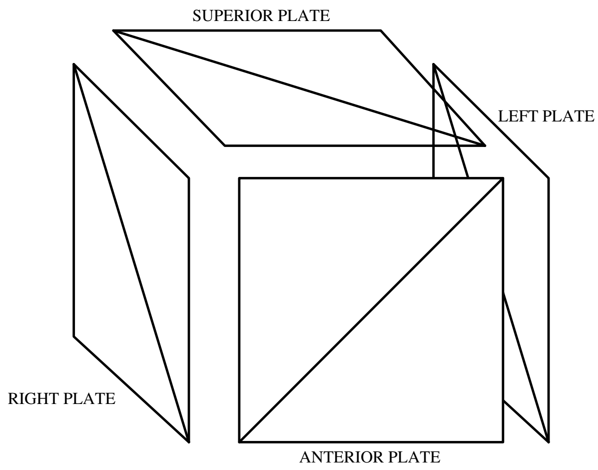

Figure 5.1: Markers of the OBT frame.

to define the *acquisition plane* as the plane formed by the frequency encoding gradient and the phase encoding gradient that changes the most rapidly. Typically, the orientation can be transverse (x-y plane), sagittal (y-z plane) or coronal (x-z plane), were x increases from left to right, y increases from anterior to posterior and z increases from inferior to superior (with respect to a patient lying supine in the scanner). This convention also defines the orientation of the plane that peels from the 3-D data block most readily, i.e., where data elements constitute a linear vector in computer memory.

Independently of the acquisition plane, the 3-D data can be viewed in any of these planes. Figs. 5.2 to 5.4 illustrate the different slice orientations with respect to the stereotactic marker structure and the appearance of the image for each case. The phantom that appears in these images was not used in the analysis, but provided a convenient way to support the frame and simulated the level of the MR signal encountered in practice.

The four corners of the squares formed by the markers in each plate constitute points that are easily localized on the image. Moreover, the position of these corners on the images can be found by fitting straight lines on each linear channel followed by finding the intersection point of the lines found in this manner.

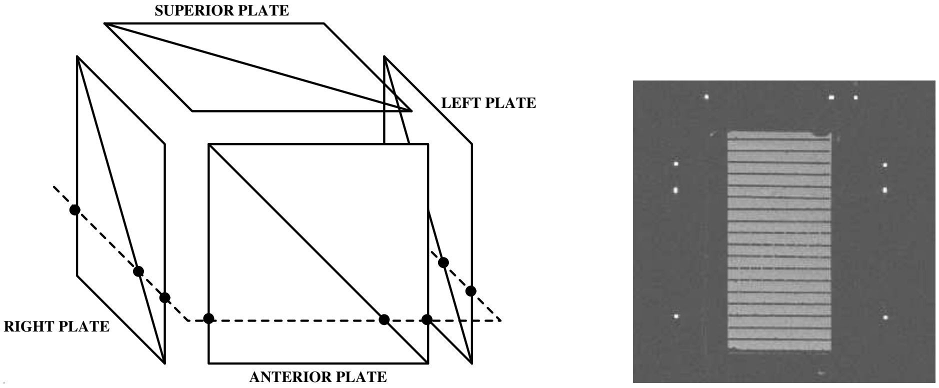

Figure 5.2: Transverse image of the OBT stereotactic frame marker structure.

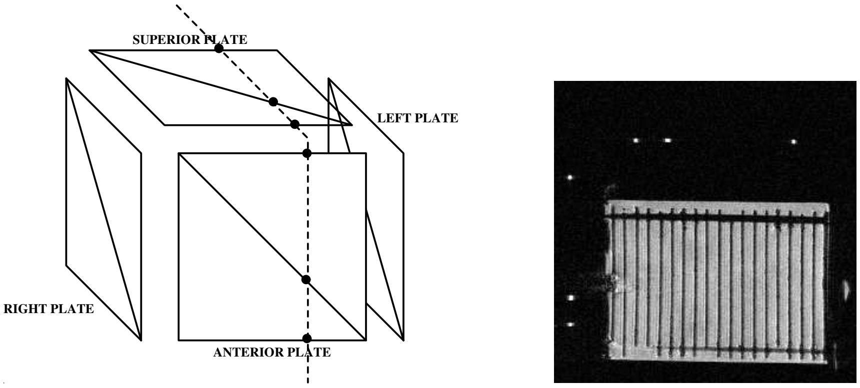

Figure 5.3: Sagittal image of the OBT stereotactic frame marker structure.

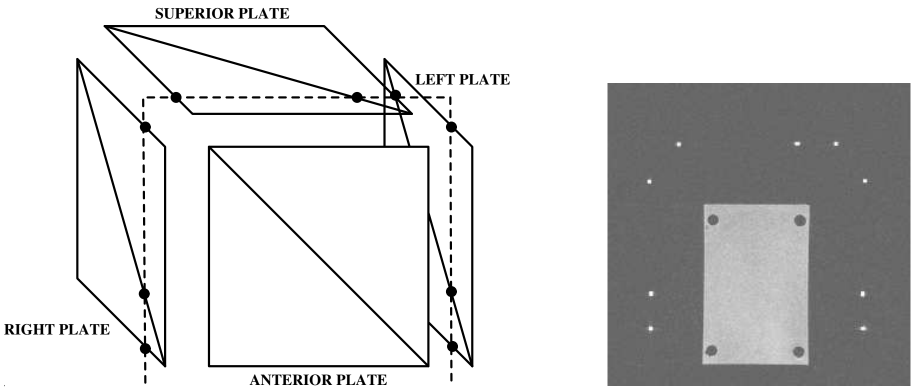

Figure 5.4: Coronal image of the OBT stereotactic frame marker structure.

5.1.1 Data acquisition

Three volumetric T1-weighted gradient-echo scans of the OBT stereotactic frame mounted on a plastic phantom filled with $CuS0_4$ solution were acquired transversely, sagittally and coronally respectively. The imaging parameters were identical for the three scans (voxel size = $1 \times 1 \times 1$ mm, echo time 10.3 ms, repetition time = 17.8 ms). The frequency encoding direction was x for the transverse acquisition and z for the other two. The left, right, superior and anterior plates were mounted on the frame.

A Matlab script was written to extract the centroids of the channel sections semi-automatically on each slice of the three data sets. The section of one particular channel is seen when the volume is viewed in a plane perpendicular to that channel. Centroids were found by computing the average of the pixel positions, weighted by the pixel values, in a square neighbourhood of the maximum pixel of the marker section (the mean background values were subtracted from the pixel values and any resulting negative pixels were set to zero).

5.1.2 Data analysis

Fitting channels to straight lines

Since each channel has the shape of a straight line, 3-D linear regression was performed on the centroid positions. A line in 3-D space can be described by the following vector equation:

$$\vec{r} = \vec{r}_0 + t\vec{u}, \tag{5.1}$$

where $\vec{r}_0 = x_0\vec{i} + y_0\vec{j} + z_0\vec{k}$ is a point vector belonging to the line, $\vec{u}$ a vector parallel to the line and t a free parameter allowing a position on the line to be specified. $\vec{i}$, $\vec{j}$ and $\vec{k}$ are the usual unit vectors in the x, y and z directions respectively. If (5.1) is written as:

$$x = m_x z + b_x, \tag{5.2}$$

$$y = m_y z + b_y, \tag{5.3}$$

standard formulae of 2-D linear regression can be used, given N 3-D points $(x_i, y_i, z_i), i = 1 \ldots N$ to be fitted, to find m_x, m_y, b_x, b_y. The vectorial equation of the line is then:

$$\vec{r} = (b_x\vec{i} + b_y\vec{j}) \ + \ t\,(m_x\vec{i} + m_y\vec{j} + \vec{k}). \tag{5.4}$$

Intersection of two channels

Once each channel has been fitted to a line, the intersection of any two channels $C1$ and $C2$ can be computed by finding the two points $\vec{a}$ and $\vec{b}$ belonging to $C1$ and $C2$ respectively such that the distance between them is the smallest possible. Let the equations of $C1$ and $C2$ be:

$$\vec{r} \;=\; \vec{r}_1 + t\vec{u}_1, \tag{5.5}$$

$$\vec{r} \;=\; \vec{r}_2 + t\vec{u}_2. \tag{5.6}$$

Since the shortest distance between a point and a line is that measured perpendicularly to the line, the shortest line segment between $C1$ and $C2$ is perpendicular to both of these lines. This can be expressed vectorially by:

$$(\vec{b} - \vec{a}) = C\ (\vec{u}_1 \times \vec{u}_2), \tag{5.7}$$

where C is a constant. Furthermore, the fact that $\vec{a} \in C1$ and $\vec{b} \in C2$ gives the equations:

$$\vec{a} \;=\; \vec{r}_1 + t_a\vec{u}_1, \tag{5.8}$$

$$\vec{b} \;=\; \vec{r}_2 + t_b\vec{u}_2, \tag{5.9}$$

which can also be written:

$$\vec{a} \times \vec{u}_1 \;=\; \vec{r}_1 \times \vec{u}_1, \tag{5.10}$$

$$\vec{b} \times \vec{u}_2 \;=\; \vec{r}_2 \times \vec{u}_2. \tag{5.11}$$

The seven scalar unknowns that constitute $\vec{a}$, $\vec{b}$ and C can be determined by using the three scalar equations given by the vectorial equation (5.7) together with the four independent scalar equations given by the vectorial equations (5.10) and (5.11).

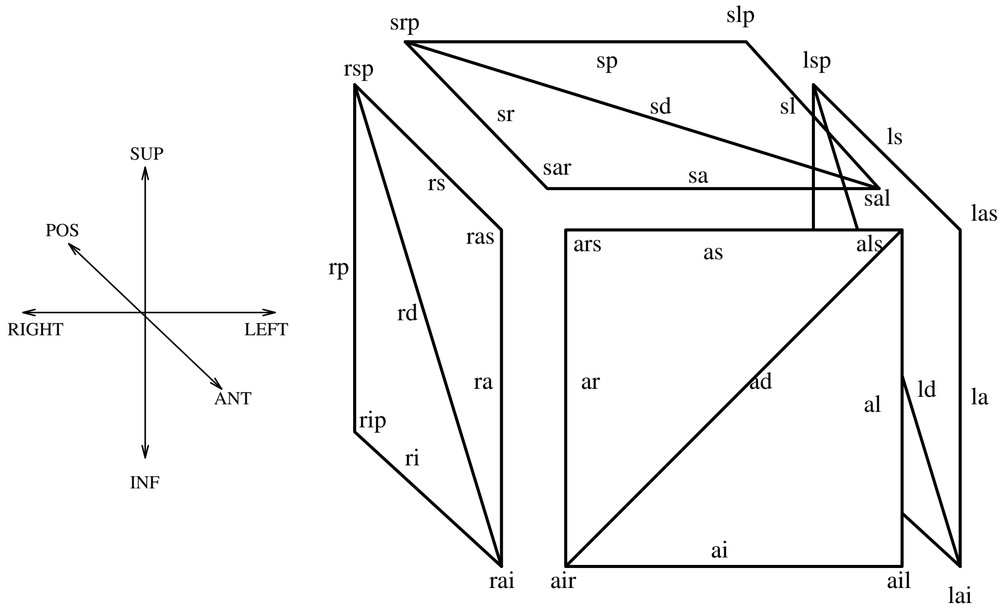

Figure 5.5: Channels and intersections labels.

5.1.3 Results

After a line was fitted to every channel, the intersections of the channels were computed using the above formalism allowing the position of the corners formed by the channels to be found. In order to identify each channel unambiguously, a labelling convention was adopted. A channel is identified by two letters: the first one refers to the plate in which it is embedded and the second letter, to the position in the plate (l = left, r = right, s = superior, i = inferior, a = anterior, p = posterior, d = diagonal). For instance, channel *li* refers to the inferior channel of the left plate and *rd* refers to the diagonal channel in the right plate. The corners of the square formed by the channels are labeled with three letters. Again, the first one refers to the plate and the other two specify the position in the plate. So, the corner *ars* specifies the right superior corner of the anterior plate. Note that when a diagonal channel is involved, three different intersections correspond to the same point. The labelling of most of the channels and intersections is shown in Fig. 5.5. The position of the channel intersections of are displayed in Table 5.1.

Referring to Table 5.1, by looking at the corners defined by more than one intersection, it is obvious that one cannot consider the uncertainty on the position of some corners to be less that

Corner	*Markers*	*Intersection (mm)*			*Distance (mm)*
		x	y	z	
ail	ad - ai	-62.16	142.18	-32.17	0.39
	ad - al	-62.39	141.90	-32.39	0.05
	ai - al	-62.39	142.15	-32.17	0.45
air	ai - ar	63.81	142.81	-32.90	0.68
als	al - as	-62.75	141.69	93.88	1.82
ars	ad - as	63.86	142.58	93.20	1.64
	ad - ar	63.25	141.73	92.57	0.31
	ar - as	63.25	142.48	93.21	1.82
lai	la - li	-86.19	84.66	-32.53	1.45
	la - ld	-86.82	84.66	-32.32	0.21
	li - ld	-86.09	84.86	-32.52	1.24
las	la - ls	-89.18	84.70	94.50	0.23
lip	li - lp	-86.84	-43.71	-34.70	1.18
lps	ld - ls	-89.45	-45.53	93.47	0.44
	ld - lp	-89.24	-45.46	93.40	0.03
	lp - ls	-89.45	-45.46	93.47	0.45
rai	ra - ri	90.68	85.64	-33.45	2.15
	ra - rd	89.76	85.65	-33.49	0.32
	ri - rd	90.81	85.57	-33.44	1.89
ras	ra - rs	89.51	85.45	93.45	1.33
rip	ri - rp	89.89	-42.80	-36.64	1.44
rps	rd - rs	89.56	-44.23	92.35	0.56
	rd - rp	89.12	-44.20	92.31	0.24
	rp - rs	89.42	-44.20	92.35	0.83
sal	sa - sd	-64.42	87.13	125.16	0.43
	sa - sl	-64.16	87.13	125.02	0.14
	sd - sl	-64.16	86.75	125.33	0.50
sar	sa - sr	66.00	87.39	124.41	0.02
slp	sl - sp	-64.17	-46.64	124.48	0.15
spr	sd - sr	65.82	-46.04	123.50	0.09
	sd - sp	65.43	-45.76	123.62	0.13
	sp - sr	65.82	-45.76	123.51	0.09

Table 5.1: Computed intersections of frame markers.

1 mm. For instance, intersection *rai* shows a difference between the three intersections of the order of 1 mm. Nevertheless, this 1 mm uncertainty is not larger than that on the position of the corners found by direct inspection of the images. This deceiving result is explainable by the fact that some markers undergo a space-variant distortion (not only a shift). This distortion suggests that the linear fit might not accurately match the position of the marker near the intersection. Moreover, the marker distortion seems to become more important near the intersection, making any extrapolation attempt uncertain. However, other intersections corresponding to the same corner present smaller differences ($\sim$ 0.5 mm), meaning that in these cases, the corner positions can be considered to be determined accurately.

Distances between various corners were computed using the data of Table 5.1, and Table 5.2 shows the difference between the known distances of the frame corners from manufacturer's specifications, and the distance computed for each acquisition. For corners defined by several intersections, the intersection between the two orthogonal channels was taken as the corner position. Note that, in order to avoid any potential error due to the misplacement of the plates on the frame, only the distance between corners embedded in the same plate were considered.

5.1.4 Conclusion

Results shown in Table 5.2 may be summarized as follows.

- The distance between the corners found from the images can differ in some cases from the actual distance of as much as 6 mm, meaning that the displacement of individual corners can be around 3 mm. However, the smallest difference found is 0.1 mm. The mean absolute differences are 2.5 mm, 3.0 mm and 3.0 mm for the transverse, sagittal and coronal acquisitions respectively.

- The distance between the corners found from the images can vary by a maximum of $\sim$ 3 mm depending of the type of acquisition. It can also be observed that the distance between the corners is similar for the sagittal and the coronal acquisitions. This can be understood by the fact that these data were acquired with the readout gradient in the same direction.

corners	*Acquisition*		
	transverse	*sagittal*	*coronal*
air-ail	3.9	3.1	3.1
als-ail	3.9	5.3	5.4
ars-air	4.0	5.7	5.8
ars-als	3.8	2.6	2.5
las-lai	3.0	5.4	5.4
lip-lai	1.6	1.5	1.6
lps-las	-0.2	-0.1	-0.1
lps-lip	2.0	4.8	5.1
rai-lai	4.3	2.7	2.5
ras-las	2.3	-0.1	-0.3
ras-rai	2.9	5.9	5.9
rip-lip	4.2	2.6	2.5
rip-rai	1.4	1.5	1.6
rps-lps	2.0	-0.4	-0.6
rps-ras	0.4	0.2	0.1
rps-rip	2.5	5.7	5.8
sar-sal	-0.1	-2.9	-2.9
slp-sal	-3.7	-3.8	-3.1
spr-sar	-3.2	-3.2	-3.2
spr-slp	-0.2	-2.6	-2.7

Table 5.2: Frame corners distortion.

Difference (mm) between the real distances of the frame corners and the distance computed for each acquisition.

> The small difference can however be attributed to eddy current effects, since the gradient switching sequence is different for the two acquisitions, and possibly to differences in linearity between the two phase encoding gradients.

This experiment shows the order of magnitude of the distortion affecting the 3-D structure formed by the markers of the OBT stereotactic frame. According to [20], the largest part of these distortions is caused by the bulk magnetic susceptibility of the frame plates. This demonstrates that special care must be taken in the design (shape and material) of any external localizing device.

It is important to underline the fact that this result does not imply that the error on the localization of points in conventional stereotaxy using the OBT frame is in the order of 5 mm. We have to keep in mind that this experiment investigated the accuracy of the representation of the stereotactic frame as a 3-D structure, whereas conventional stereotaxy localization only relies on information found on one slice.

5.2 Field Mapping

Another issue that is of interest in IGNS is patient-induced susceptibility distortion, which can be important wherever a sharp variation in the magnetic susceptibility is present. Although magnetic susceptibility variations may not be significant deep inside the brain, they can constitute a real problem near the surface of the skin or near bone-air interfaces at the skull-base. Since many registration techniques rely on the use of surface structures, it is important to assess potential errors of this nature.

The goal of this section is to investigate the possibility of using the three-point Dixon imaging technique [22, 21] to acquire magnetic field maps of a human subject. The field map gives a direct representation of the static field inhomogeneity, allowing the measurement of the spatial misregistration associated with each point of an image. Typically, such a field map can be obtained by computing the phase difference between two images acquired with different echo times.

In order to understand how this works, consider a general 2-D Fourier image acquisition. The received signal, after low pass filtering can be written:

$$s(t) = A \int_x \int_y \rho(x,y) e^{-\imath\omega(x,y)t} dy\, dx, \tag{5.12}$$

where ρ is the weighted spin density, and A, a proportionality constant. This equation expresses the fact that the signal can be considered as a superposition of harmonic oscillators whose frequencies and amplitudes are space-variant.

For a typical spin echo sequence (Fig. 5.6), the phase distribution, including the effect of main field inhomogeneity $\Delta B(x,y)$, can be written:

$$\theta(x,y,t) = \omega(x,y)t = -\gamma \int_0^{\frac{T_{SE}}{2}} \left[\vec{G}(\tau)\cdot\vec{r} + \Delta B(x,y)\right]\, d\tau + \gamma \int_{\frac{T_{SE}}{2}}^{t} \left[\vec{G}(\tau)\cdot\vec{r} + \Delta B(x,y)\right]\, d\tau, \tag{5.13}$$

where

$$\vec{G} = (G_x, G_y)\ , \qquad \vec{r} = (x,y), \tag{5.14}$$

γ is the gyromagnetic ratio and G_x and $G_y = ngy$ the magnetic field gradient in the x and y

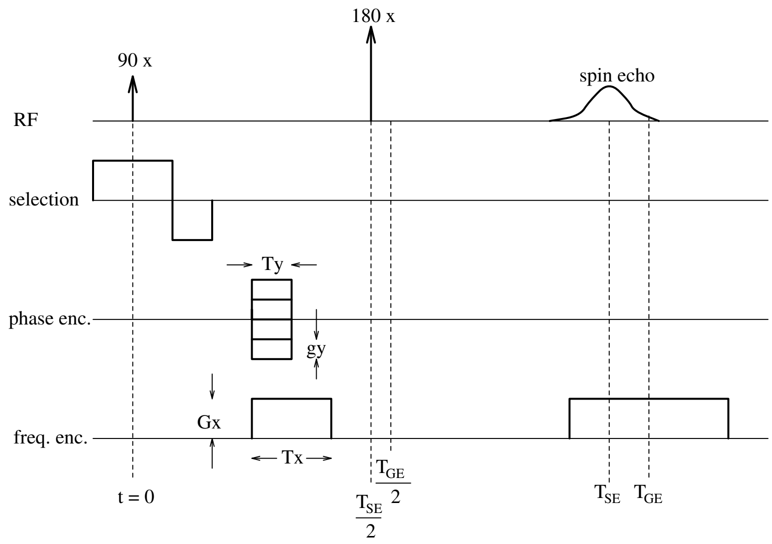

Figure 5.6: Spin-echo sequence with the gradient echo not aligned with the spin-echo.

directions respectively. gy represents the increment unit of the phase encoding gradient amplitude. The first term in (5.13) represents the phase distribution immediately after the application of the $180°$ pulse[a].

The evaluation of (5.13) for the sequence of Fig. 5.6 gives:

$$\theta(x, y, t) = \gamma G_x x(t - T_{GE}) - \gamma G_y T_y + \gamma \Delta B(x, y)(t - T_{SE}), \tag{5.15}$$

By letting $\Delta T \equiv T_{SE} - T_{GE}$, this becomes:

$$\theta(x, y, t) = \gamma \left[(G_x x + \Delta B(x, y)) (t - T_{GE}) - G_y T_y - \Delta B(x, y) \Delta T . \right] \tag{5.16}$$

Replacing the last equation in Equation (5.12) we obtain for the signal $s(t)$:

$$\begin{aligned} s(t) &= A \int_x \int_y \rho(x, y) e^{\imath\gamma \Delta B(x,y) \Delta T} e^{-\imath\gamma[(G_x x + \Delta B(x,y))(t - T_{GE}) - G_y T_y]} dy\, dx \\ &= A \int_x \int_y \rho(x, y) e^{\imath\gamma \Delta B(x,y) \Delta T} e^{-2\pi\imath\left[k_x (x + \frac{\Delta B(x,y)}{G_x}) + k_y y\right]} dy\, dx, \end{aligned} \tag{5.17}$$

where

$$k_x = \frac{\gamma}{2\pi} G_x (t - T_{GE}) \qquad \text{and} \qquad k_y = -\frac{\gamma}{2\pi} G_y T_y . \tag{5.18}$$

[a] If the phase was θ just before the reversing pulse, it becomes $-\theta$ after if the $180°$ pulse is around the x-axis. This assumes that the phase angle is measured with respect to the x-axis.

It can be seen from the (5.17) that the reconstructed image $\rho'(x, y)$ (by inverse Fourier transform) will be:

$$\rho'(x, y) = \rho(x, y)e^{\imath\gamma\Delta B(x,y)\Delta T}. \tag{5.19}$$

So, if the gradient echo and the spin echo coincide ($\Delta T = 0$), which is normally the case, the reconstructed image is real. Otherwise, the reconstructed image contains a phase factor that depends on the field inhomogeneity $\Delta B(x, y)$. In theory, as shown by Equation (5.19), only one image would be necessary to reconstruct the field map. However in practice, other sources of dephasing are present and it is desirable to subtract the phases of two images acquired with different ΔT in order to keep only contributions to the dephasing that are due to field inhomogeneities.

Another problem is encountered in reality. Since the precession frequency of protons in fat is slightly lower than that of protons in water, fat protons can be interpreted as water protons in a different (lower) magnetic field. If ω_{cs} is the difference between the precession rate of protons in fat and in water, the corresponding field offset is $\Delta B_{cs} = -\omega_{cs}/\gamma$. This can be expressed mathematically by writing the reconstructed image as the sum of contributions from fat and water:

$$I = \left(\rho_W + \rho_F e^{-\imath\omega_{cs}\Delta T}\right) e^{\imath\gamma\Delta B\Delta T}. \tag{5.20}$$

If one were to acquire a field map, the extra phase factor associated with the fat signal would be impossible to distinguish from that associated with field inhomogeneities.

The *two-point Dixon technique* [14] allows the water and fat signals to be separated. The principle of this technique is to acquire two images, one (I_0) with $\Delta T = 0$, and the other (I_+) with $\Delta T = \pi/\omega_{cs}$ (this implies that the reversing pulse must be applied $\Delta T/2$ earlier as that in a normal spin-echo acquisition). From (5.20) the equation of the two images is:

$$I_0 = (\rho_W + \rho_F), \tag{5.21}$$

$$I_+ = (\rho_W - \rho_F), e^{\imath\phi} \tag{5.22}$$

where $\phi \equiv \pi\gamma\Delta B/\omega_{cs}$. In the absence of field inhomogeneity ($\phi = 0$), the fat and water images are given by:

$$\rho_W = (I_0 + I_-)/2, \tag{5.23}$$

$$\rho_F = (I_0 - I_-)/2. \tag{5.24}$$

Otherwise, the presence of inhomogeneities makes the exact separation of water and fat images impossible. Note that ϕ cannot be obtained from $\arg(I_+)$ since the sign of $(\rho_W - \rho_F)$ is not known.

5.2.1 Three-point Dixon technique

The *three-point Dixon technique* [22] extends the above method by adding a third acquisition (I_-) with $\Delta T = -\pi/\omega_{cs}$. The three acquisitions can be written:

$$\begin{aligned} I_- &= (\rho_W - \rho_F)\, e^{-\imath\phi(x,y)} e^{\imath\theta} && (5.25) \\ &= M_- e^{\Phi_-}, \\ I_0 &= (\rho_W + \rho_F)\, e^{\imath\theta} && (5.26) \\ &= M_0 e^{\Phi_0}, \\ I_+ &= (\rho_W - \rho_F)\, e^{\imath\phi} e^{\imath\theta} && (5.27) \\ &= M_+ e^{\Phi_+}, \end{aligned}$$

where the M's and the Φ's represent the modulus and the phase of the acquired images and θ is a phase shift common to all three acquisitions. This phase factor is easy to remove since it is equal to Φ_0. Let

$$\begin{aligned} S_- &= I_- e^{-\imath\Phi_0} \\ &= (\rho_W - \rho_F)\, e^{-\imath\phi}, && (5.28) \\ S_0 &= I_0 e^{-\imath\Phi_0} = M_0 \\ &= (\rho_W + \rho_F)\,, && (5.29) \\ S_+ &= I_+ e^{-\imath\Phi_0} \\ &= (\rho_W - \rho_F)\, e^{\imath\phi}. && (5.30) \end{aligned}$$

The third acquisition makes it possible to determine ϕ since:

$$I_+ I_-^* = |\rho_W - \rho_F|^2 e^{2\imath\phi} \Rightarrow \phi = \frac{\Phi_+ - \Phi_-}{2} \tag{5.31}$$

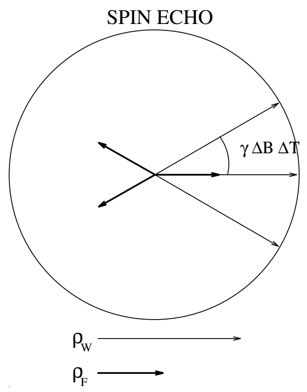

Figure 5.7: Phase relation in three-point Dixon technique with spin-echo acquisition.

Since the argument of $I_+ I_-^*$ is only unambiguous between $-\pi$ and π, ϕ can be determined directly from the last equation only if it is between $-\pi/2$ and $\pi/2$. This would require the size of the field inhomogeneity to be smaller than $\omega_{cs}/(2\gamma)$ which is certainly not acceptable. However, under the assumption that the gradient of the inhomogeneity-induced phase shift is limited to a certain value, it is possible to *unwrap* the phase, i.e., to find the phase from its principal value between $-\pi$ and π. A method for unwrapping the phase is presented by Glover and Schneider [22]. Song et al. [57] also present a technique to unwrap the phase by solving the Poisson equation with appropriate boundary conditions.

Once ϕ is known, by unwrapping $\Phi_+ - \Phi_-$ and dividing by two, the water and fat images can easily be obtained. Letting

$$R_0 = \frac{1}{2}\left(S_+ e^{-\imath\phi} + S_- e^{\imath\phi}\right), \tag{5.32}$$

we find:

$$\rho_W = \frac{1}{2}\left(S_0 + R_0\right) \tag{5.33}$$

$$\rho_F = \frac{1}{2}\left(S_0 - R_0\right) \tag{5.34}$$

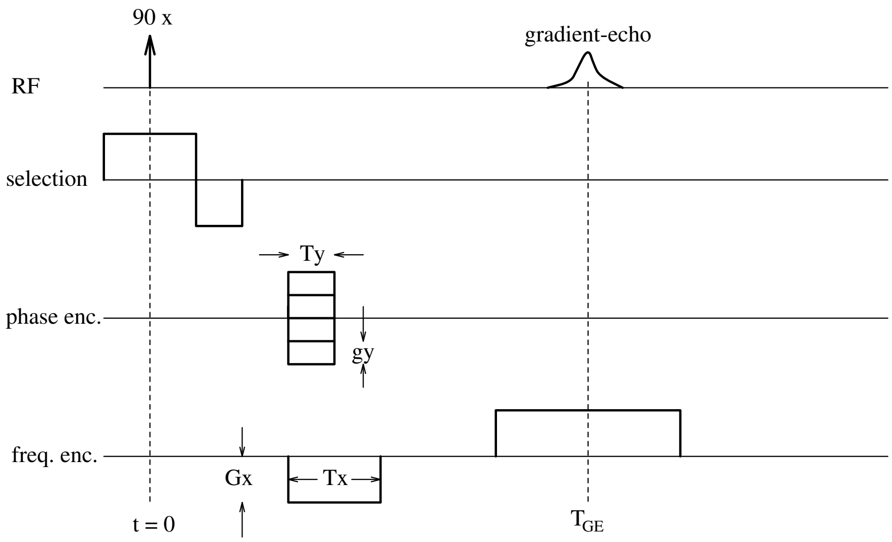

Figure 5.8: Typical gradient-echo sequence.

Three-Point-Dixon using gradient-echo

Using the same argument as previously, it can be shown that the reconstructed density produced by a gradient-echo acquisition (Fig. 5.8) can be written:

$$I = \left(\rho_W + \rho_F e^{i\omega_{cs}\mathrm{TE}}\right) e^{-i\gamma\Delta B\mathrm{TE}}, \tag{5.35}$$

where TE is the echo time. Comparing with (5.19), this shows clearly that gradient-echo, as opposed to spin-echo images, contain a "natural" phase factor. In other words, gradient-echo acquisition does not remove the effect of field inhomogeneities.

Again, consider three acquisitions (I_-,I_0,I_+) with echo time of TE $-\,\Delta T$, TE and TE $+\,\Delta T$ respectively. Choosing ΔT so that $\omega_{cs}\Delta T = \pi$, the three acquisitions are given by:

$$\begin{aligned} I_- &= \left(\rho_W - \rho_F e^{\imath\omega_{cs}\mathrm{TE}}\right) e^{-\imath\gamma\Delta B\mathrm{TE}} e^{\imath\phi} e^{\imath\theta} && (5.36)\\ &= M_- e^{\imath\Phi_-} \\ I_0 &= \left(\rho_W + \rho_F e^{\imath\omega_{cs}\mathrm{TE}}\right) e^{-\imath\gamma\Delta B\mathrm{TE}} e^{\imath\theta} && (5.37)\\ &= M_0 e^{\imath\Phi_0} \\ I_+ &= \left(\rho_W - \rho_F e^{\imath\omega_{cs}\mathrm{TE}}\right) e^{-\imath\gamma\Delta B\mathrm{TE}} e^{-\imath\phi} e^{\imath\theta} && (5.38)\\ &= M_+ e^{\imath\Phi_+} \end{aligned}$$

where θ is a phase shift common to all acquisitions. It can be shown that the water and fat images are given by:

$$\rho_W = \frac{1}{2}\sqrt{(R_- + R_+) + \sqrt{(R_- + R_+)^2 - (R_- - R_+)^2/\sin^2(\omega_{cs}\mathrm{TE})}} \tag{5.39}$$

$$\rho_F = \frac{1}{2}\sqrt{-(R_- + R_+) + \sqrt{(R_- + R_+)^2 - (R_- - R_+)^2/\sin^2(\omega_{cs}\mathrm{TE})}} \tag{5.40}$$

Note that these equations break down when ω_{cs}TE is an integer multiple of π. In these situations however, (5.36) to (5.38) reduce to (5.25) to (5.27) with the sign of ϕ reversed and with an extra constant phase factor that can be included in θ. So, one can always choose the echo-time of a gradient-echo sequence so that the simpler equations of the spin-echo case can be used to compute the water and fat images.

5.2.2 Results

A set of three spin-echo acquisitions was obtained. One of these was a standard sequence, whereas the other two were performed with the $180°$ pulse shifted in time by $\pm$ 1.12 ms. The phase and magnitude images of the three acquisition are shown in Fig. 5.9.

The shifted phase images were unwrapped using the technique described by M. Song [57], who provided us with his computer program.

Even though the acquisition of the field map does not require the computation of the water and fat images, their equations have been derived in last section as a means of double checking the field map obtained, since an incorrect field map cannot lead to separation of fat and water. The water, fat and field map images were computed using these equations, and are shown in Fig. 5.10. Fig. 5.11 shows the same field map as in Fig. 5.10 but the gray-scale explicitly relate to the value, in ppm, of the field inhomogeneity displayed.

A similar set of images were acquired using a gradient-echo sequence. The first was measured with a TE of 11.2 ms and the other two, with a TE of 8.96 ms and 13.44 ms respectively. Note that the echo time of the intermediate image is such that $\sin(\omega_{cs}\mathrm{TE}) = 0$. The resulting water, fat and field images are shown in Fig. 5.12.

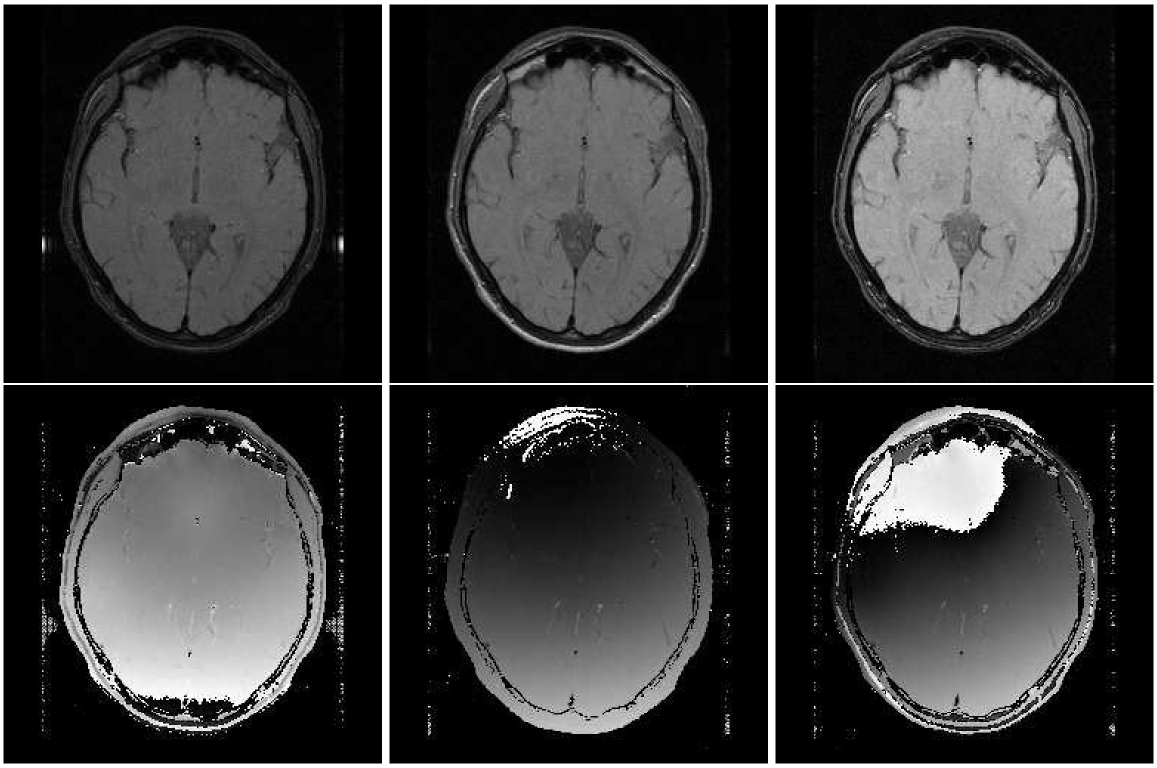

Figure 5.9: Three-point Dixon spin-echo acquisitions.

Magnitude (top) and phase (bottom) images. The leftmost (rightmost) images were obtained by shifting the reversing pulse by -1.12 ms (+1.12 ms). The center images were acquired with a standard spin-echo sequence.

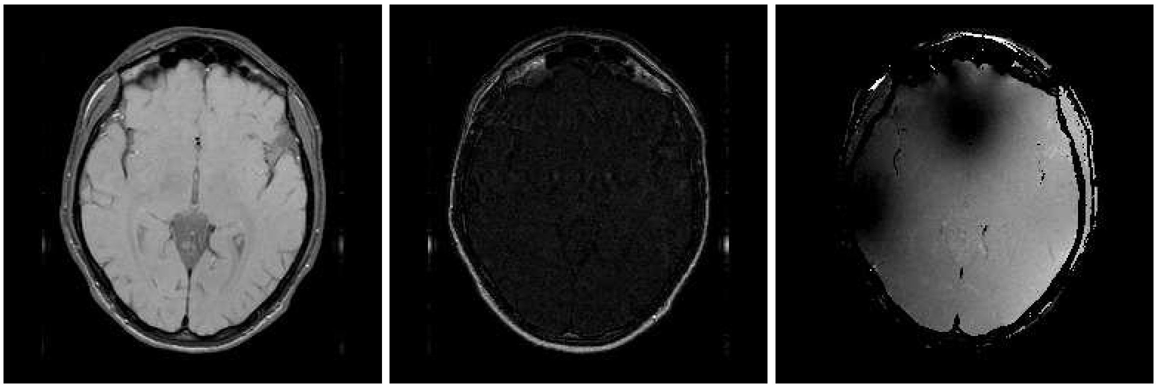

Figure 5.10: Three-point dixon results for spin-echo images.

Water (left), fat (middle) images and field map (right). As expected, signal from fat is almost inexistent inside the brain but is more important on the skin. This shows that fat suppression is essential to get an accurate field map on the skin regions. Without fat suppression, it would be difficult to distinguish between field inhomogeneity and phase shift of fat.

Observe that the field map actually determined can be affected by eddy currents which are dependant of the MR pulse sequence used. For instance, a gradient-echo sequence with short TE will be affected differently by eddy currents than a spin-echo sequence with long TE.

5.2.3 Conclusion

The results that have been presented here are highly dependant on the accuracy of phase unwrapping procedure. For all images tested, the unwrapping process in the brain region was almost always successful, but problems were encountered for in thin region defined by the skin. So, more work is required to perform perfect unwrapping of the phase over skin-regions.

Another problem experienced was movement during acquisition, causing the three-point Dixon technique to fail whenever a geometrical inconsistency was found between the three images. While we had to acquire the three images in three separate acquisitions, an appropriately interleaved acquisition (unavailable to us) could alleviate this problem. In our case, a rather long time interval (in the order of 2-3 minutes) in between the three scans of the three-point Dixon

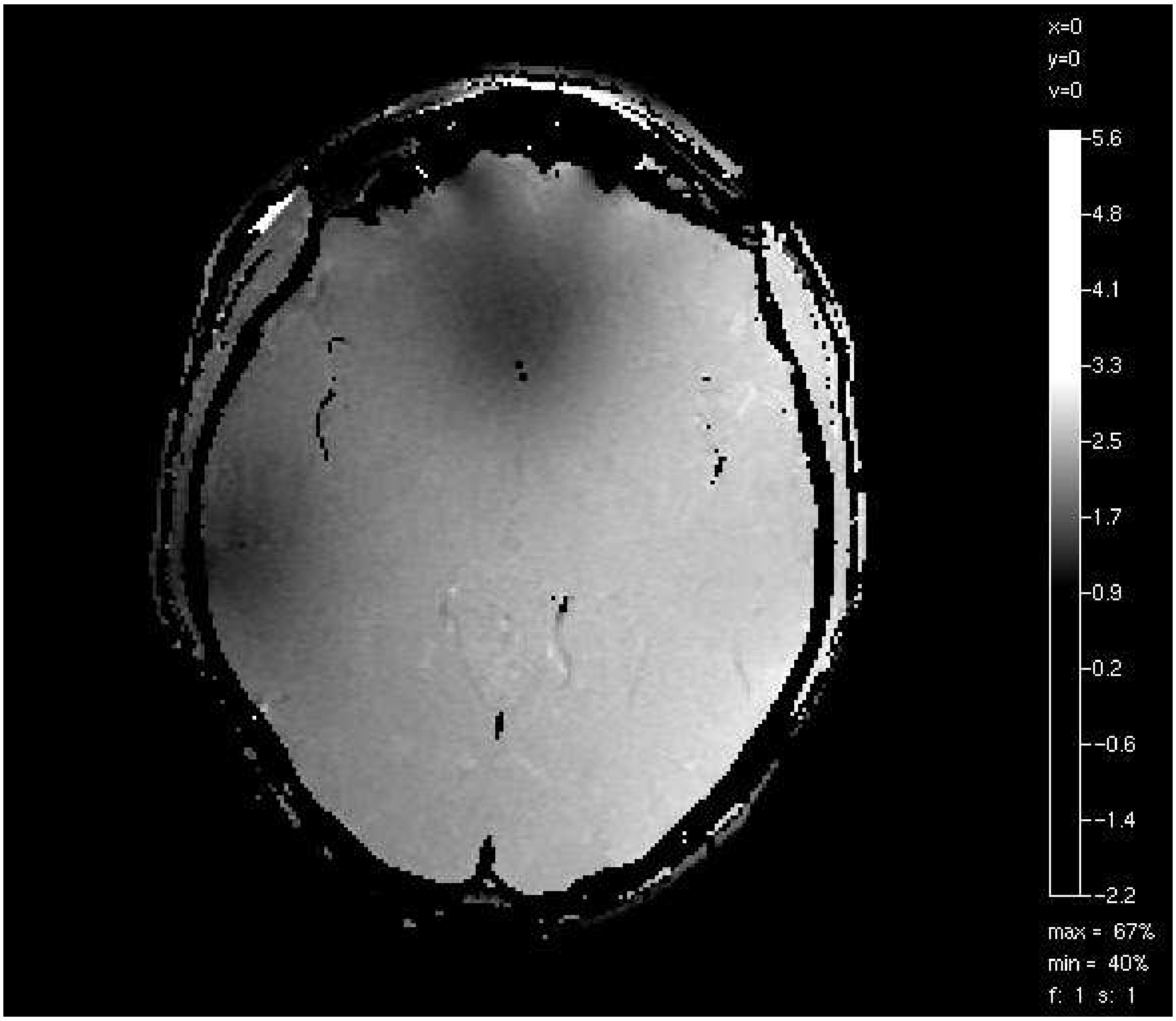

Figure 5.11: Field map from spin-echo sequence.

The numbers on the grey-scale are the values of the field inhomogeneity in ppm (parts per million). The magnitude of the frequency encoding gradient is given in term of the water-fat shift in pixels (we used a water-fat shift of two pixels for this acquisition). So, these numbers can be converted in spatial shift in pixels, knowing that the precession frequency difference between water and fat is $\omega_{cs} = 3.5$ ppm. For this acquisition then, the spatial shift (in pixels) at any point is given by $2\Delta B/3.5 = 0.57\,\Delta B$, where ΔB is given in ppm.

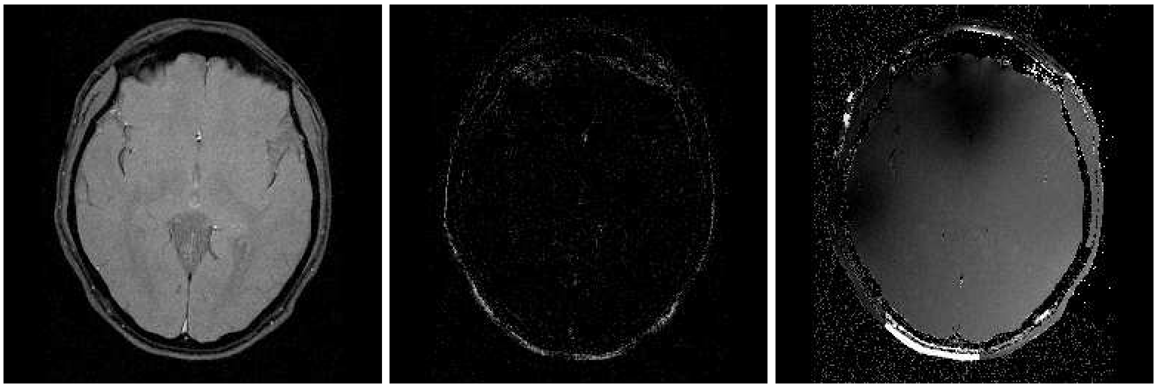

Figure 5.12: Three-point dixon results for gradient-echo images.

Water (left), fat (middle) images and field map (right).Although more noisy than images from spin-echo acquisitions, these images demonstrate that the three-point-Dixon technique can be used with gradient echo images. Note the close similarity of the field map with the one found with spin-echo sequence even though the bottom left portion of the skin was not successfully unwrapped. TE was chosen so that $\sin(w_{cs}\mathrm{TE}) = 0$. Equation (5.33) and (5.34) have been used to reconstruct the image.

technique, made the movement difficult to avoid.

Because of these factors, it was difficult to perform quantitative analysis of the field offset caused by susceptibility effects at the air-skin interface. We feel however that a better unwrapping and a suitable acquisition sequence will make it possible.

Chapter 6

Conclusion and Future work

IGNS is a vast subject, and the purpose of the work described in this thesis was to begin to address the issue of accuracy.

Some of the aspects of this topic are discussed here but a large number of questions are still unanswered. The contributions of this work on the understanding of the accuracy problems in IGNS and suggestions for further work in this area, are discussed below.

In Chapter 2 a general model of IGNS was introduced. This model presented the image acquisition, the digitizing of the patient's head and the registration as being the links between various spaces involved in IGNS, and clearly showed how the various elements of IGNS interact with each other to produce the overall result.

It was shown in Chapter 3 that the calculation of the RMS registration error over a large number of registrations can be a useful technique to characterize the performance of different registration methods or different conditions of application of the same registration method. Moreover this method has the advantage of characterizing the variation, over the volume of the head, of the registration error.

The comparison between homologous point matching and surface matching registration techniques did not give the accuracy of each in absolute terms but allowed a good impression to be obtained of the order of magnitude of the registration errors that can occur in a real clinical situation. Moreover, it was demonstrated that a small rotational error can cause the registration error to rapidly increase with the distance from the center of the head. The large differences observed between homologous point and surface matching registrations can in part be explained by the reasons below.

- The corners of the frame markers that were used for the homologous point matching can be significantly distorted on MR images (as shown in Chapter 5).
- The corners of the markers, due to the stereotactic frame design, are nearly in the same plane. According to Zinreich *et al.* [67], this can make the homologous point registration less accurate. Moreover, only four homologous point pairs were used while it is preferable to use more.
- The frame is not optimally designed to be used with a localizing device such as the FARO surgical arm. Since the markers are embedded within plastic plates, it was not physically possible to reach the corners with the probe.

In addition, comparisons between a small number of homologous point registrations using the marker intersections of the stereotactic frame have demonstrated that the variability of this technique is significantly less than that of registrations performed by surface matching.

Simulations described in Chapter 3 showed that a sub millimetric accuracy over the whole field of view can be achieved, in noisy situations, by using a large number of homologous points (see, for example, Figs. 3.5 and 3.6). Since it is difficult in practice to find more than half of a dozen landmarks well defined on both the patient and the image, the only way to identify a larger number of homologous points is to use extrinsic landmarks. An MR distortion experiment (Chapter 5) showed however that the use of such extrinsic structures for registration must be approached with care. Susceptibility effects can introduce shifts that may substantially reduce the registration accuracy (but does not affect the precision, i.e., the variability from one registration to the other). Moreover, the fact that the registration error decreases as the square root of the number of homologous point pairs used implicitly assumes that the error on the localization of the points is random. However, distortion due to susceptibility effects can introduce non-random errors that would make the use of a large number of fiducial landmarks ineffective in reducing the registration error.

The use of the three-point Dixon technique for the acquisition of field maps has been illustrated and it has been shown to be potentially useful in the determination of patient-induced field inhomogeneities. Its efficient use requires however that a special pulse sequence be implemented, which is not the case at the MNI. Also, more work needs to be performed in order to obtain a better phase unwrapping over the region of the skin.

The accuracy of the localizing device (the FARO surgical arm) used at MNI, was assessed by a simple experiment using a mechanical "gold standard" described in Chapter 4. In addition, the accuracy of another localizing device, the OPTOTRAK, was measured by the same technique. The result have shown that the OPTOTRAK gave distances both closer to the true values and with less variability, with its average accuracy having been evaluated as ~ 0.09 mm with a maximum error on the distance measured of 0.18 mm. The average accuracy of the FARO arm was evaluated as ~ 0.25 mm, with a maximum error of 0.57 mm, which is acceptable considering the present level of accuracy observed in IGNS.

6.1 Future Work

6.1.1 Characterization of absolute registration error

This thesis presents various measurements of the difference between registrations but the lack of a gold standard registration technique did not allow us to consider the registration error in absolute terms. A registration performed using the stereotactic frame markers, such as described in Chapter 3, was shown to be more stable than a surface fit registration, but because of the problems outlined in the last section, its accuracy was not sufficient to be considered as a reference technique.

We believe however that it is possible to achieve this result by slightly modifying the OBT stereotactic frame. For example, holes in which the tip of the probe would precisely fit could be drilled at various locations on the frame. Additionnally, spherical markers could also be fixed to the frame, at accurately known positions relative to the holes, and whose coordinates could be precisely determined by finding their centroids on images. Furthermore, MRI experiments could be performed to characterize any distortion undergone by these markers. This approach would allow very accurate registrations to be performed, and absolute registration error measurement to be acheived.

6.1.2 Use of a localizer

Graphs of the RMS registration error in Chapter 3 clearly shows that the accuracy of a registration is greatly increased by the use of a large number of landmarks. In the OR context however, the length of time available to perform the registration procedure is limited. Moreover, few natural landmarks are subject to good localization in both spaces. This makes it impractical to use a large number of landmarks for a registration if each of these points must be identified on both the patient and the image.

One approach that could partially solve this problem is the usage of some "localizer" that would consist of a large set of small MR-visible markers fixed permanently to a rigid support, and whose relative positions would be known precisely. We could imagine for instance, the localizer as being a sort of "helmet" in which the markers are embedded. This helmet could be rigidly mounted on a light-weight ring that would be attached to the patient's head. The separation between the localizer and the attachment (i.e., the ring) would allow it to be removed after the scan is performed.

A careful design of the markers would allow the precise determination of their centres in image space. For instance, Sumanaweera *et al.* [60] report a technique allowing the determination of the marker localization to a precision better that one tenth of a pixel. Analysis of the field distortion caused by the markers and the support would also increase the localization precision by allowing correction for susceptibility shift. Moreover, marker identification can be performed automatically since the computer knows the marker configuration *a priori*.

If landmarks, which can be unambiguously reached with the probe and whose positions relative to the set of markers on the helmet are accurately known, are built on the attachment, the registration procedure would be limited to identifying these landmarks on the ring. The known position of the markers on images could be used to correct for the non-linear distortion that can be present in the imaging data. Note that the helmet would be only needed during the image acquisition. Only the attachment would be required for registration before the surgery, reducing the patient discomfort to a minimum.

6.1.3 Optimization of MR pulse sequences

Even though there are techniques allowing volumes to be warped non-linearly [7, 9, 8], it is still a better approach to try to produce distortion-free images. Several MR image distortion correction methods require the acquisition of two images. This double acquisition can lead to unacceptable scan times since IGNS requires a large number of slices. Work has still has to be performed for the development of clinically applicable pulse sequences that produce geometrically accurate images in reasonable times.

6.1.4 Real time monitoring of anatomical changes

The model presented in Chapter 2 did not discuss the fact that the transformation $\mathbf{R}$ may be rapidly time varying after the opening of the skull. Leakage of CSF and the surgical intervention itself are certainly factors causing the shape of the patient's anatomy to change during the time the surgery is performed. Several approaches have been proposed to perform a real-time monitoring of anatomical changes during the surgery. Among others are interventional MR imaging [50, 32], ultrasound [35], video [26]. These techniques will themselves present challenging accuracy issues.

Bibliography

[1] C.H. An, C.G. Atkeson, and J. M. Hollerbach. *Model Based Control of a Robot Manipulator*. MIT Press, Cambridge, MA, 1988.

[2] K. S. Arun, T. S. Huang, and S. D. Blostein. Least-squares fitting of two 3-D point sets. *IEEE Transactions on Pattern Analysis and Machine Intelligence*, 9(5):698–700, September 1987.

[3] G. H. Barnett, D. W. Kormos, C. P. Steiner, et al. Frameless stereotaxy using a sonic digitizing wand: Development and adaption to the picker vistar medical imaging system. In R. J. Maciunas, editor, *Interactive Image-guided Neurosurgery*, pages 113–119. American Association of Neurological Surgeons, 1993.

[4] Fred L. Bookstein. Principal warps: Thin-plate splines and the decomposition of deformations. *IEEE Transactions on Pattern Analysis and Machine Intelligence*, PAMI-11(6):567–585, 1989.

[5] R. D. Bucholz and K. R. Smith. A comparison of sonic digitizers versus light emitting diode-based localization. In R. J. Maciunas, editor, *Interactive Image-guided Neurosurgery*, pages 179–200. American Association of Neurological Surgeons, 1993.

[6] H. Chang and J.M. Fitzpatrick. Geometrical image transformation to compensate for mri distortions. In *SPIE Vol. 1233 Medical Imaging IV: Image Processing*, 1990.

[7] D. L. Collins. *3D model-based segmentation of individual brain structures from magnetic resonance imaging data*. PhD thesis, McGill University, Montreal, Canada, 1994.

[8] D. L. Collins, W. Dai, T. S. Marrett, and A. C. Evans. Three-dimensional non-linear warping of a computerized volume-of-interest brain atlas for morphometric analysis. In *Information Processing in Medical Imaging*, Wye, UK, July 1991. poster session.

[9] D. Louis Collins, Terry M. Peters, and Alan C. Evans. An automated 3D non-linear image deformation procedure for determination of gross morphometric variability in human brain. In *Proceedings of Third Conference on Visualization in Biomedical Computing*, volume 2359, pages 180–190. SPIE, Oct. 4-7 1994.

[10] R. Damanian. Tumor detection by NMR. *Science*, 171(1151), 1971.

[11] Bruce Davey, Roch Comeau, Chris Gabe, Andre Olivier, and Terence Peters. Interactive stereoscopic image-guided neurosurgery. In *Proceedings of SPIE Medical Imaging*, volume 2164, pages 167–176. SPIE, 1994.

[12] Bruce Davey, Patrice Munger, Roch Comeau, Laura Pisani, Andre Olivier, and Terry Peters. Applying stereoscopic image visualization to neurosurgical image guidance. In Anthony M. DiGioia, Takeo Kanade, and Russell Taylor, editors, *Proceedings of the First International Symposium on Medical Robotics and Computer Assisted Surgery*, pages 264–271, Pittsburgh, Penn., September 22-24 1994. Shadyside Hospital.

[13] Bruce L. K. Davey, Roch M. Comeau, Patrice Munger, Laura J. Pisani, Daniel Lacerte, Andre Olivier, and Terence M. Peters. Multimodality interactive stereoscopic image-guided neurosurgery. In Richard A. Robb, editor, *Proceedings of Third Conference on Visualization in Biomedical Computing*, volume 2359, pages 526–536. SPIE, SPIE, Oct. 4-7 1994.

[14] W. Thomas Dixon. Simple proton spectroscopic imaging. *Radiology*, 153:189–194, 1984.

[15] J.M. Drake, J. Prudencio, and S. Holowka. A comparison of the PUMA robotic system and the ISG viewing wand for neurosurgery. In *Interactive Image-Guided Neurosurgery*. American Association of Neurological Surgeons, 1993.

[16] A. C. Evans, T. M. Peters, D. L. Collins, P. Neelin, and C. Gabe. Image registration based on discrete anatomical structures. In R.J. Maciunas, editor, *Interactive image-guided neurosurgery*, chapter 5, pages 63–80. American Association of Neurological Surgeons, 1993.

[17] R. L. Galloway and R. J. Maciunas. An articulated localizing arm for neurosurgical use. In R.J. Maciunas, editor, *Interactive image-guided neurosurgery*, pages 159–168. American Association of Neurological Surgeons, 1993.

[18] R. L. Galloway, R. J. Maciunas, and James W. Latimer. The accuracies of four stereotactic frame systems: An independent assessment. *Biomedical Instrumentation and Technology*, 25:457–460, 1991.

[19] R. L. Galloway Jr., R. J. Maciunas, and C. A. Edwards II. Interactive image-guided neurosurgery. *IEEE Transactions on Biomedical Engineering*, 39(12):1226–1231, Dec 1992.

[20] A. Gauvin. Geometrical distortion of magnetic resonance images. Master's thesis, McGill University, May 1992.

[21] G.H. Glover. Multipoint dixon technique for water and fat proton and susceptibility imaging. *Journal of magnetic resonance imaging*, 1(5), 1991.

[22] G.H. Glover and E. Schneider. Three-point Dixon technique for true water/fat decomposition with b_0 inhomogeneity correction. *Magnetic Resonance in Medicine*, 18, 1991.

[23] H. Goldstein. *Classical Mechanics*. Addison-Wesley, Reading, MA, 1981.

[24] A. Goshtasby. Piecewise cubic mapping functions for image registration. *Pattern Recognition. Sciences*, 1971.

[25] A. Goshtasby. Piecewise linear mapping functions for image registration. *Pattern Recognition*, 1986.

[26] M. P. Heilbrun, P. McDonald, C. Wiker, S. Koehler, W. Peters Y. Sieminov, and C. Wiker. Implementation of a machine vision method for stereotactic localization and guidance. In

R. J. Maciunas, editor, *Interactive Image-guided Neurosurgery*, pages 169–178. American Association of Neurological Surgeons, 1993.

[27] C. J. Henri, D. L. Collins, and T. M. Peters. Multi-modality image integration for stereotactic surgical planning. *Medical Physics*, 18(2):167–177, Mar/Apr 1991.

[28] Chris Henri. Application of stereoscopic digital subtraction angiograms to stereotactic neurosurgery planning. Master's thesis, McGill University, Montreal, September-October 1989.

[29] V. Horsley and R.H. Clarke. The structure and functions of the cerebellum examined by a new method. *Brain*, 31:45–124, 1908.

[30] G.N. Hounsfield, J. Ambrose, B.J. Perry, and C. Bridges. Computerized transverse axial scanning (tomography). *Brittish Journal of Radiology*, 46:1016–1051, 1973.

[31] Northern Digital Inc. *Technical Product Description: OPTOTRAK*. Northern Digital Inc., 1991.

[32] A.F. Jolesz. Interventional magnets and systems. In *Proceedings of the Society of Magnetic Resonance in Medicine*, volume 2, page 409, 1994.

[33] A. Kato, T. Yoshimine, T. Hayakawa, Y. Tomita, T. Ikeda, M. Mitomo, K. Harada, and H. Mogami. A frameless, armless navigational system for computer-assisted neurosurgery. technical note. *Journal of Neurosurgery*, 74(5):845–9, May 1991.

[34] D. Kondziolka, P. K. Dempsey, L. D. Lunsford, J. R. W. Kestle, E. J. Dolan, E. Kanal, and R. R. Tasker. A comparason between magnetic resonance imaging and computed tomography for stereotactic coordinate determination. *Neurosurgery*, 30:402–407, 1992.

[35] P. Kumar, R. Sukthankar, B. J. Damany, J. Mishra, and A. N. Jha. Evaluation of intraoperative ultrasound in neurosurgery. *Annals of the Academy of Medicine, Singapore*, 22(3 Suppl):422–7, May 1993.

[36] P. C. Lauterbur. Image formation by induced local interactions: Examples using nuclear magnetic resonance. *Nature*, 242:190–191, 1973.

[37] L. Leksell. A stereotaxic apparatus for intracerebral surgery. *Acta Chir Scand*, 99:229–233, 1949.

[38] L. Lemieux, N. D. Kitchen, S. W. Hughes, and D. G. T. Thomas. Voxel-based localization in frame-based and frameless stereotaxy and its accuracy. *Medical Physics*, 21:1301–1310, 1994.

[39] K.O. Lim and A. Pfefferbaum. Segmentation of MR brain images into cerebrospinal fluid spaces, white and grey matter. *Journal of Computer Assisted Tomography*, 13(4), 1989.

[40] C. R. Maurer Jr. and J. M. Fitzpatric. A review of medical image registration. In R. J. Maciunas, editor, *Interactive Image-guided Neurosurgery*, pages 17–44. American Association of Neurological Surgeons, 1993.

[41] J. Michiels, H. Bosmans, P. Pelgrims, D. Vandermeulen, J.Gybels, G. Marchal, and P. Suetens. On the problem of geometric distortion in magnetic resonance images for stereotactic neurosurgery. *Magnetic Resonance Imaging*, 12(5), 1994.

[42] P. Neelin, J. Crossman, D. J. Hawkes, Y. Ma, and A. C. Evans. Validation of an MRI/PET landmark registration method using 3D simulated PET images and point simulations. *Computerized Medical Imaging and Graphics*, 17(4-5):351–6, Jul-Oct 1993.

[43] J. Oikarinen, J. Alakuijala, Y. Louhisalmi, S. Sallinen, H. Helminen, and J. Koivukangas. The oulu neuronavigator system: Intraoperative ultrasonography in verification of neurosurgical localization and visualization. In *Interactive Image-Guided Neurosurgery*. American Association of Neurological Surgeons, 1993.

[44] C. A. Pelizzari and G. T. Y Chen. Registration of multiple diagnostic imaging scans using surface fitting. In I.A.D Bruinvas et al, editor, *The Use of Computers in Radiation Therapy*. Elsevier Science Publishers B.V., North-Holland, 1987.

[45] C. A. Pelizzari, G. T. Y. Chen, D. R. Spelbring, R. R. Weichselbaum, and C. T. Chen. Accurate three-dimensional registration of CT, PET and MRI images of the brian. *Journal of Computer Assisted Tomography*, 13(1):20–26, 1989.

[46] Charles A. Pelizzari, David N. Levin, George T. Y. Chen, and Chin-Tu Chen. Image registration based on anatomical surface matching. In R.J. Maciunas, editor, *Interactive image-guided neurosurgery*, chapter 4, pages 47–62. American Association of Neurological Surgeons, 1993.

[47] T. M. Peters, B. L. K. Davey, P. Munger, R. M. Comeau, A. Evans, and A. Olivier. Three-dimensional multi-modal image-guidance for neurosurgery. submitted to IEEE Transactions on Medical Imaging, 1994, 1994.

[48] T. M. Peters, C. J. Henri, A. Olivier, and L. Lemieux. Experience with a computerized stereoscopic workstation for neurosurgical planning. In *Proceedings of Conference on Visualization in Biomedical Computing*. IEEE, May 1990.

[49] D. W. Roberts, E. M. Friets, J. W. Strohbehn, and T. Nakajima. The sonic digitizing microscope. In *Interactive Image-Guided Neurosurgery*. American Association of Neurological Surgeons, 1993.

[50] P.B. Roemer, J.F. Schenck, F.A. Jolesz, E.T. Laskaris, and R.W. Newman. A system for MRI-guided interventional procedures. In *Proceedings of the Society of Magnetic Resonance in Medicine*, volume 2, page 420, 1994.

[51] Lothar R. Schad, Robert Boesecke, Wolfgang Schlegel, Gunther H. Hartmann, Volker Sturm, Ludwig G. Strauss, and Walter J. Lorenz. Three dimensional image correlation of CT, MR, and PET studies in radiotherapy treatment planning of brain tumors. *Journal of Computer Assisted Tomography*, 11(6):948–954, 1987.

[52] G. Schlondorff, R. Mosges, and L. Klimek. An articulated localizing arm for otolaryngology. In *Interactive Image-Guided Neurosurgery*. American Association of Neurological Surgeons, 1993.

[53] L. Shizhe, J.A. Gilmore, Q.X. Yang, and M.B. Smith. Three dimensional finite element calculations of magnetic susceptibility effects in high resolution anatomical models of human head. In *Proceedings of the Society of Magnetic Resonance*, volume 2, page 831, 1994.

[54] Robin Sibson. Studies in the robustness of multidimensional scaling: Procrustes statistics. *J. R. Statist. Soc.*, 40(2):234–238, 1978.

[55] Robin Sibson. Studies in the robustness of multidimensional scaling: Perturbation analysis of classical scaling. *J. R. Statist. Soc.*, 41(2):217–229, 1979.

[56] A. Simmons, P. S. Tofts, G. J. Barke, and S. R. Arridge. Sources of intensity nonuniformity in spin echo images at 1.5T. *Magnetic Resonance in Medicine*, 32:121–126, 1994.

[57] S. M. Song, S. Napel, N.J. Pelc, and G.H. Glover. Phase unwrapping of MR phase images using Poisson equation. to be published, 1994.

[58] E.A. Spiegel, H.T. Wycis, and M. Marks. Stereotaxic apparatus for operations on the human brain. *Science*, 106:349–350, 1947.

[59] T. Sumanaweera. Magnetic susceptibility distortion of cylindrical fiducials. supplied by author, 1992.

[60] T. Sumanaweera, G. Glover, S. Song, J. Adler, and S. Napel. Quantifying MRI geometric distortion in tissue. *Magnetic Resonance in Medicine*, 31, 1994.

[61] J. Talairach, M. David, P. Tournoux, H. Corredor, and T. Kvasina. *Atlas d'Anatomie Stéréotaxique.* Masson et Cie, Paris, 1957.

[62] ISG Technologies. *Allegro user's manual*. Missisauga, Ont., Canada.

[63] Ovitt T.W., Capp P.M., Fisher D.H., Frost M.M., Lebel J.L., Nudleman S., and Roehrig K. The development of digital video substraction systems for intravenous angiography. *Proc. SPIE*, 169, 1978.

[64] E. Watanabe. The neuronavigator: A potentiometer-based localizing arm system. In R.J. Maciunas, editor, *Interactive image-guided neurosurgery*, pages 135–147. American Association of Neurological Surgeons, 1993.

[65] S Webb, editor. *The Physics of Medical Imaging*. IOP Publishing Ltd, Bristol, England, 1988.

[66] M. Yanagisawa, S. Shigemitsu, and T. Akatsuka. Registration of locally distorted images by multiwindow pattern matching and displacement interpolation. *IEEE Proc 7th Int Conf Pattern Recognition*, 1984.

[67] S. J. Zinreich, S. Tebo, D. M. Long, H. Brem, D. Mattox, M. E. Loury, C. Vander Volk, W. Kotch, D. W. Kennedy, and R. N. Bryan. Frameless stereotactic integration of CT imaging data. *Radiology*, 188(3):735–742, September 1993.